Examining Particulate Matter Emissions from Vehicular Traffic in an Urban Environment

RHYTHM REET

A THESIS SUBMITTED TO
THE FACULTY OF GRADUATE STUDIES
IN PARTIAL FULFILLMENT OF THE REQUIREMENTS
FOR THE DEGREE OF

MASTER OF SCIENCE

GRADUATE PROGRAM IN EARTH AND SPACE SCIENCE
YORK UNIVERSITY
TORONTO, ONTARIO

June 2024

ABSTRACT

This research investigates the complexities of particulate matter (PM) emissions in urban environments, with a focus on non-exhaust sources like brake and tire wear, primarily caused by vehicular traffic in an urban area. By examining the variance in PM size, specifically particles sizes between 50 nm and 1000 nm, the study assesses the impact of traffic volume and patterns on PM emissions in Toronto, Ontario. The approach used is based on vertical fluxes measured with eddy-covariance, counting vehicles and estimation of the footprint. In this study variations in vehicle traffic were linked to fluctuations in particle concentrations and turbulent fluxes. Higher vehicle rates in weekday evenings did not correspond with increased particle numbers, whereas weekday mornings experienced higher concentrations, possibly due to overnight pollutant accumulation and the rising atmospheric boundary layer. Larger particles were more likely to originate from background sources than the road itself, particularly in areas affected by stop-and-go traffic. Over a specific week in March, however, road emissions significantly contributed to particle concentrations, a deviation from the norm. Weekends presented consistent particle deposition, suggesting that roads act more as sinks than sources, especially during periods with fewer vehicles. The complexities of urban particulate dynamics were highlighted, indicating that larger particles are prone to settle on the road surface, and changes in traffic patterns can transform typical emission sources into particle sinks. This study lays the groundwork for future research, emphasizing the need for detailed traffic data to better understand emission sources and implications for urban air quality and public health.

ACKNOWLEDGEMENTS

I would like to express my deepest gratitude to Dr. Gordon for the profound support and guidance throughout my career at York University. Throughout my undergraduate and graduate studies, Dr. Gordon's immense knowledge, invaluable advice, patience, and unwavering support have been instrumental in my success.

I owe profound thanks to my parents for their endless love and support throughout my life, but especially during my university career. Thank you for always encouraging me in all my pursuits, inspiring me, and continuously pushing me to follow my dreams. Cheers to this and many more major milestones to come.

Finally, a special thank you to my colleague and friend, Eric Ward, who has been with me throughout my studies at York University. Your encouragement, patience, and readiness to review my work have provided invaluable suggestions that improved my work.

TABLE OF CONTENT

LIST OF ABBREVIATIONS

CI: Confidence Interval

CPC: Condensation Particle Counter

EC: Eddy Covariance

EF: Emission Factor

EV: Electric Vehicle

FFP: Footprint Flux Prediction

HDV: Heavy Duty Vehicle

LDV: Light Duty Vehicle

LES: Large Eddy Simulation

LPD: Lagrangian Particle Dispersion

LPDM-B: Lagrangian Stochastic Particle Dispersion Model

OPC: Optical Particle Counter

PM: Particulate Matter

SE: Standard Error of Mean

UHSAS: Ultra-High Sensitivity Aerosol Spectrometer

LIST OF TABLES

LIST OF FIGURES

Chapter 1: Introduction and Background

Road traffic emissions are a major contributor to pollution in urban cities. Particulate matter (PM) causes millions of premature deaths worldwide, annually [Roser., 2021]. The most important exposure zone for elevated cardiopulmonary health risks is within 30m of a roadway, while the greatest risk of adverse respiratory symptoms is to those living within 300 m of a freeway [Bruge et al., 2013]. Previous studies summarized in Matthaios et al., 2022 have examined the relationship between road dust, coarse sized concentration and fine concentration, mass, and distance from the road. These studies showed a reduction in particulate matter up to 4% for particles ranging from 0.2µm to 2.5µm ($PM_{0.2-2.5}$) with distance, while elements linked to traffic related sources (i.e., Cu, Ba, Zr) exhibited greater reductions, between 20 and 60%. For North Americans, this affects a large majority of people. In Toronto, 45% of the population in lives within 500m of an expressway or 100m from a busy road [Health Effect Institute., 2010]. Understanding the amount of emissions from traffic is necessary to develop a mitigation strategy to improve air quality in urban areas.

Traffic-related emissions are a complex mixture originating from both direct vehicular tailpipe and non-direct vehicle emissions. These emissions are classified into two categories: exhaust emissions with particulates of 30 nm to 500 nm and non-exhaust emissions which are greater than 500 nm [Conte and Contini, 2019]. Exhaust emissions form in the engine during the combustion event, whereas non-exhaust emissions originate from brake wear, tire wear, and road dust resuspension. Prior studies summarized in Hagino et al (2016), concluded that acceleration, deceleration, and braking patterns, which largely arise during congestion, increase non-exhaust emission. The size of non-exhaust emissions measured in this study ranges between 500 nm to

1000 nm. Vehicle types, speed and braking patterns play a role in the type and amount of particulate matter released. This work investigates the variability of non-exhaust emissions from urban fleets, including light-duty (LDV) and heavy-duty vehicles (HDV), and quantifies the amounts of aerosols measured at a roadside location in Toronto, Ontario. Furthermore, this work investigates the size distribution of particles near a roadway, relating this to the traffic variability. This serves a proof of concept to see if it's possible to measure turbulent flux due to the diffusion of the emitted particles.

1.1: Particle Size Classifications

To comprehensively understand vehicle emissions, it is crucial to investigate the various aerosol sizes and their modes. This investigation provides insights into their behavior and transport mechanisms in the atmosphere. Particles can be described in terms of surface area per particle, particle number, mass, or concentration within an aerosol volume (Kwon et al., 2020). Most often, PM is described by number concentration and mass concentration.

There are three main size distributions discussed in this research: coarse, fine, and ultrafine particles. Coarse and fine particles are typically described according to their mass distribution, whereas ultrafine particles, having negligible mass, are quantified by number concentration due to their dominance in particle count.

Coarse PM, also referred to as PM_{10}, has diameters ranging from 2.5 μm ($PM_{2.5}$) to 10 μm (PM_{10}). Fine PM are particles with diameters of 2.5 μm ($PM_{2.5}$) or less. Ultrafine PM (UFP) are particles with diameters of 0.1 μm (100 nm) or less, dominating in ambient air by particle number. The greatest concern about UFPs is their ability to reach the deepest lung regions and bypass primary airway defenses [Kwon et al., 2020].

PM_{10} and $PM_{2.5}$ also have harmful systemic health effects. $PM_{2.5}$ has been linked to premature death, particularly in individuals with chronic heart or lung diseases, and reduced lung function growth in children, whereas long-term exposure to PM_{10} has been associated with respiratory mortality (California Air Resources Board).

Table 1 compares the surface area of particles with different diameters based on the diagram provided in Kwon et al. (2020). The diagram assumes all particles are perfect spheres, have the same density, and are present in equal mass amounts. The mass, particle number, and surface area of coarse particles are arbitrarily designated as one, and other values are relative to the coarse particle.

Particles exist in three modes: nucleation mode, accumulation mode, and coarse mode. These modes influence particle growth, the formation of new particles, and how long particles remain suspended in the atmosphere (Figure 1). Particle concentrations are highest near the ground and decrease with height because most sources are near the ground and gravitational settling, along with wet deposition, are the main removal processes. The rate of settling increases with particle size, and residence time is influenced by both settling velocity and processes that act as particle sinks [Oke et al., 2017].

Nucleation mode corresponds to particles formed from gaseous molecules, which then grow via condensation and coagulate with other nucleated particles (K.R. Spurny, 1998). Nucleation mode includes particles less than 50 nm in size. The higher number and larger surface area for a given mass concentration in this mode promote condensation and coagulation processes. Sources of nucleation mode particles include combustion events, gas-to-particle conversion, and photochemical reactions, with sinks comprising coagulation and capture by cloud particles [Oke et al., 2017]. These particles have the shortest residence time, typically less than an hour [Oke et al., 2017].

Accumulation mode includes particles between 0.1 μm and 1 μm, resulting from emissions of fine particles (combustion) and dynamic events such as condensation and coagulation [Kwon et al., 2020]. The name "accumulation mode" reflects the longer residence time of these particles. Removal mechanisms are least efficient for this fraction, causing particles to accumulate and remain in the atmosphere for days to weeks [Kwon et al., 2020; Oke et al., 2020]. They are ultimately removed via wet or dry deposition [Oke et al., 2020].

The final mode is coarse mode, consisting mostly of large particles emitted through mechanical processes such as industrial activities, dust, or construction particles [McMurry et al., 2004; Oke et al., 2017]. These particles are removed from the atmosphere primarily through wet deposition, dry deposition, and gravitational settling, as they have the greatest settling velocity.

Table 1: Comparison of surface area of particles with different diameters. The diagram assumes all particles are perfect spheres, have the same density, and are present in equal mass amounts. The mass, particle number, and surface area of coarse particles are arbitrarily designated as one, and other values are relative to the coarse particle.

	COARSE (10 µm)	FINE (2.5 µm)	ULTRAFINE (0.1 µm)
		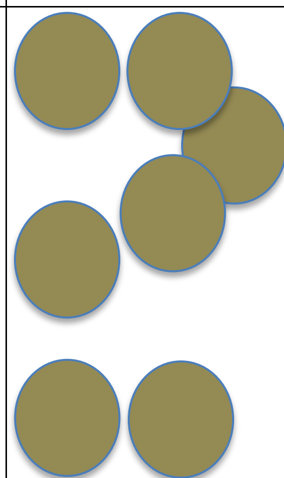	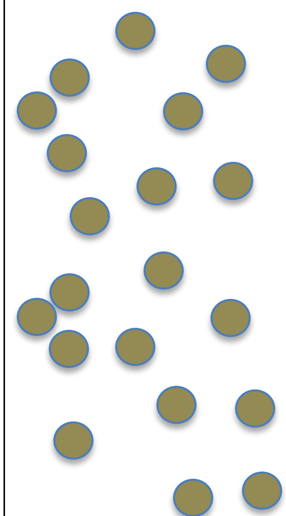
Total Mass	1	1	1
Particle Number	1	64	1,000,000
Surface Area	1	0.0625	0.0001
Total surface area per mass	1	4	100

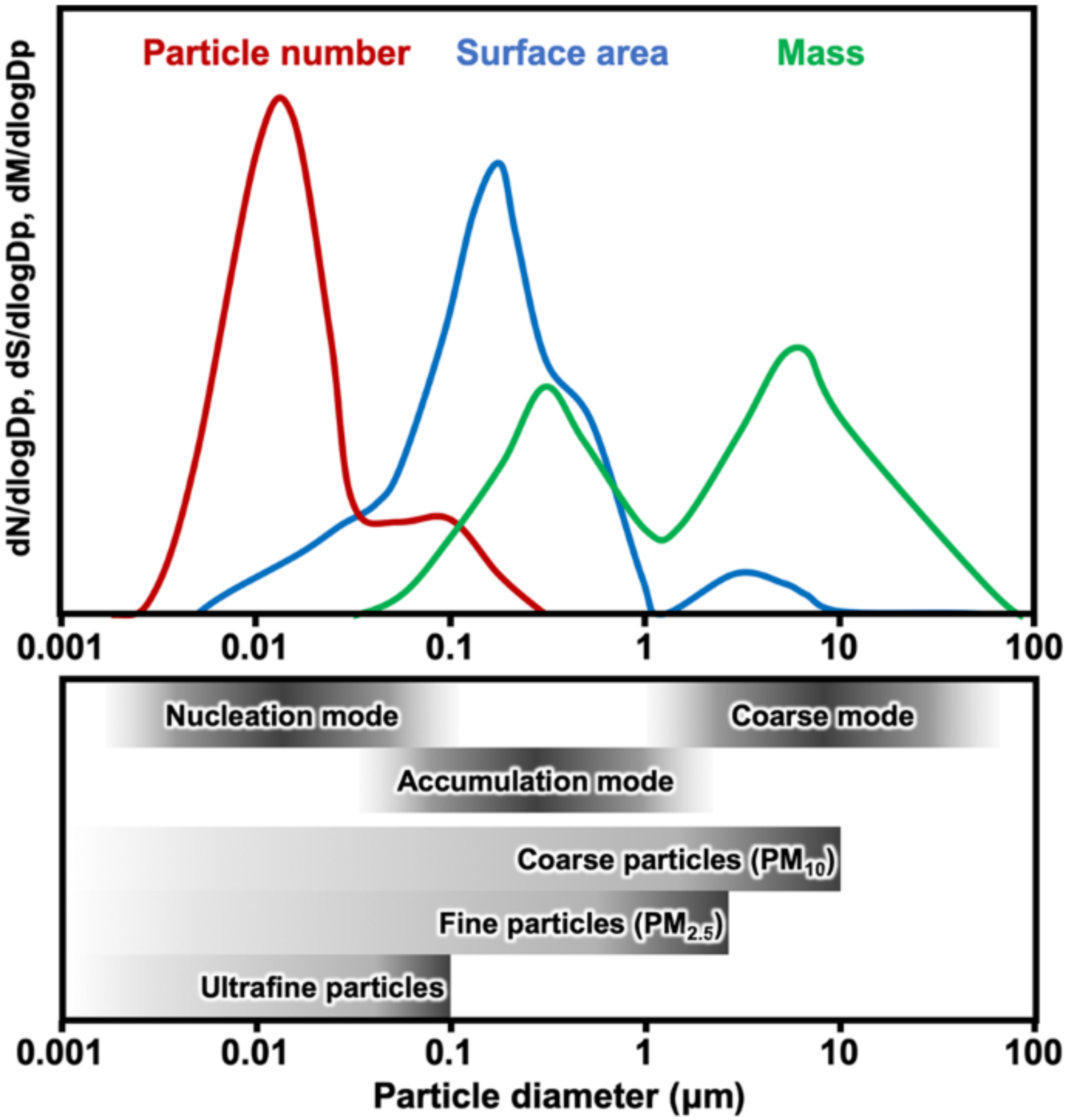

Figure 1: A) Schematic representation of a typical particle-size distribution of the number concentration, surface area concentration, and mass concentration (dN/dLog Dp, particle number per cubic millimeter; dS/dLog Dp, particle surface area per cubic millimeter) from Kwow et al.(2020). B) Schematic of the aerosol size distribution in the three modes. Ultrafine particles (UFPs) are all particles with a diameter of 100nm or less. Most nucleation mode particles and the fraction of accumulation mode particles are UFPs but can go up to PM_{10}. Graphic from Kwow et al., 2020.

1.2: Non-Exhaust Emissions

Non-exhaust emissions are an accumulation of fragments from tire wear, brake wear, and the resuspension of road dust. They are mainly larger particles with a diameter greater than 600 nm; however, many studies have recognized that a consistent fraction of non-exhaust particles have diameters smaller than 100nm [Conte and Contini., 2019]. Tire wear particles are generated by shear force between the tire tread and the road surface and are predominantly coarse, jagged and rough particles [Pant and Harrison., 2013]. Brake wear, including abrasion lining material and brake discs, is created from the grinding of brake pad constituents, or volatilization and condensation of brake pad materials known to release PM directly into the atmosphere. Finally, road dust consists of primarily coarse-sized particles derived from different origins such as traffic and industrial emissions. [Pant and Harrison., 2013]. In order to understand the contribution and overall impact of road traffic emissions to the environment, it is important to understand the various aspects including source, quantitative contribution, and emission characteristics.

1.2.1: Brake Wear

During forced deceleration, the contact between components of the brake system generates friction, which is a significant contributor to the release of particulate matter by vehicles. Braking actions lead to the degradation of both the brake lining materials and the brake disc or drum. The extent of the wear primarily depends on the composition of the linings employed and the driving conditions that subject the brakes to stress. The investigation of the physical properties of brake wear particles takes into account a wide range of brake lining materials on the market that influence brake wear. Thorpe and Harrison (2008) described the five main components:

- Fibers - comprising between 6% and 35% of brake lining mass. Fibers provide mechanical strength and are made from various metals, carbon, glass, and Kevlar.
- Abrasives - accounting for 10% of the lining material. They serve to increase friction, maintain cleanliness between contact surfaces and limit the build-up of transfer films.
- Lubricants - comprising 5-29% of the brake lining, and assisting in stabilising fractional properties, especially at high braking temperature.
- Fillers - The percentage of composition can fluctuate between 15-70% and they are incorporated to reduce manufacturing costs and improve manufacturability.
- Binders -comprising for 20-40%, they are important for maintaining structural integrity of the brake lining under mechanical and thermal stresses.

The emissions and composition of brake wear particles vary depending on a number of factors: a) brake friction material parameters, b) brake assembly type, including discs, drums, assembly sizes, surface structures, and depth of the grooves and c) vehicle operating conditions, including initial speed, deceleration, pressure, torque, and brake temperature. In tests conducted in street canyon traffic and at urban background sites, it was found that brake wear particles in $PM_{2.5}$, with a size of 2.5 µm, emissions have two peaks that coincide with rush hour traffic, suggesting brake wear is more prevalent during those times [Hagino et.al., 2016]. Garg et al. (2000) used a brake dynamometer on seven lining formulations widely used in US fleets in 2000 and concluded that on average 86% of the emitted airborne brake particles were PM_{10} (particles sized 10 µm), 63% were $PM_{2.5}$ and 33% were $PM_{0.1}$ (particles sized 100 nm) [Thorpe and Harrison., 2008]. However, based on emission factors for brake wear used in the

EMEP/CORINAIR Emissions Inventory Guidebook in 2004, it was calculated that only 8% of the emitted airborne brake particles were $PM_{0.1}$, significantly less than Grag et. al (2000). On average only 30-50% of brake wear particles become airborne [Hagino et.al., 2013].

In the field, it is challenging to determine emissions resulting from varying speeds and the force of braking and accelerating. Hagino et al (2013) assessed brake wear emission components under driving cycles that represent real-world driving conditions. The measured exhaust emissions were correlated with time, speed, and braking events, with the test conducted over 10 runs. Conducted in Japan, the study used vehicles that are commonly seen on the roads there. Vehicles I and II represent standard passenger cars to analyze disc brake systems, while Vehicle III represents a middle-class truck to analyze drum brake systems.

In North America, most passenger vehicles and bikes use disc brakes, specifically hydraulic disc brakes, while transport trucks use air brakes. Drum brakes are common in commercial vehicles, such as trucks. The results from this study are presented in Figure 2. The first run represents a cold start exhaust test, where the engine operates below its normal temperature, resulting in lower PM emissions. Run #10 corresponds to a hot start, with the engine operating at normal temperatures. The time-resolved exhaust emission profiles for PM10 and $PM_{2.5}$ were similar, particularly for Vehicle III, which showed nearly identical levels of PM_{10} and $PM_{2.5}$ emissions [Hagino et al., 2016]. This suggests that both fine particles (< 2.5 μm) and coarse particles (2.5–10 μm) are significant components of brake wear particles [Hagino et al., 2016].

In Figure 2, the brake flag represents braking patterns, where a shorter length indicates a quick, intense brake, and a longer length indicates a slower, gentler brake. Two peak types were found: one during the application of a braking force and one during wheel rotation for Vehicles I and II [Hagino et al., 2016]. The first peak was observed during a braking event (Fig. 2) and indicated that brake wear particles were generated from the collision and friction between the disc and the pads [Hagino et al., 2016]. The second peak occurred during rotor rotation and acceleration (Fig. 2), suggesting that brake wear particles, including ultrafine particles, appeared even when the rotor was spinning before the onset of braking [Hagen et al., 2019; Hagino et al., 2016; Iiijima et al., 2007; Park et al., 2021; Thomas et al., 2024]. For Vehicle III with the drum brake (Fig. 2c), only one type of peak was observed from applying the braking force. The peak increase started with the application of the braking force (Fig. 2), with slight emissions during driving with a rotating rotor [Hagino et al., 2016].

The observed airborne brake wear particle emissions ranged from 0.04 to 1.4 mg/km/vehicle for PM_{10}, and from 0.04 to 1.2 mg/km/vehicle for $PM_{2.5}$ [Hagino et al., 2016]. Two important observations from the study are: “Not all brake wear particles were emitted as airborne particles, and the mass of wear particles did not correspond to airborne PM emissions” [Hagino et al., 2016]. “The proportion of brake wear debris collected as airborne brake wear particles was 2–21% of the mass of wear” [Hagino et al., 2016]. This indicates that a significant portion of the particles are likely retained on the wheel, in the brake housing, or deposited on friction surfaces [Thorpe and Harrison, 2008; Hagino et al., 2013]. This further demonstrates that in congested areas, consistent and rapid braking increases the peak of PM emissions more than slow, gradual braking.

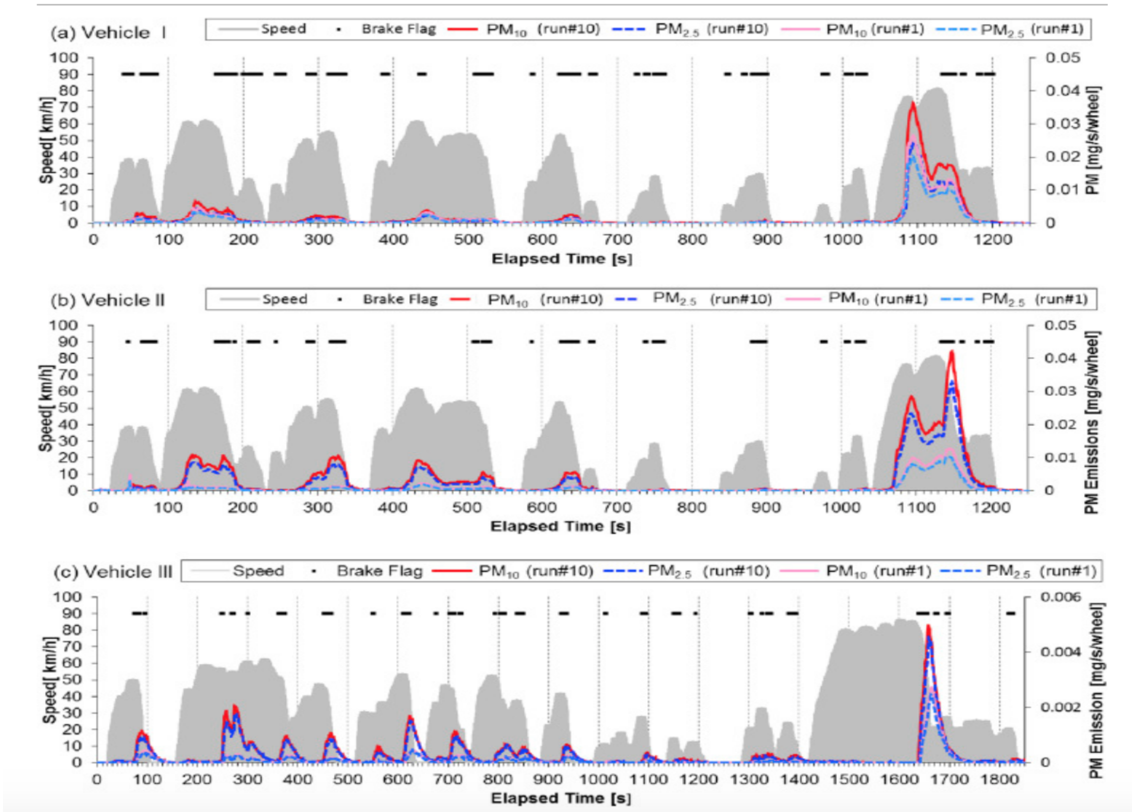

Figure 2: "Time series profiles of brake wear particle mass emissions of PM_{10} (red line = run #10/pink line = run #1) and $PM_{2.5}$ (dashed dark blue line = run #10/dashed light blue line = run #1) during transient driving test cycles: (a) vehicle I; (b) vehicle II; and (c) vehicle III. Grey shading denotes vehicle speed and black squares denote braking flags. (For interpretation of the references to colour in this figure legend, the reader is referred to the web version of this article.)" [Hagino et al.2016].

1.2.2: Tire Wear

Tire wear is a significant contributor to large particulate matter (PM) emissions (>500 nm in size), with an annual loss of rubber from tires in the UK estimated to be 53×10^6 kg (Thorpe and Harrison, 2008). Frictional contact between the road surface and tire tread results in the abrasion of the tire tread and the emission of particles into the atmosphere. Tire abrasion is primarily a mechanical process involving car acceleration and braking, and it is often assumed that emitted tire wear particles are mainly larger than 2.5 µm. However, tire wear is also influenced by multiple factors including the properties of the tire, road structure, vehicle characteristics and conditions, and driving style (Baensch-Baltruschat et al., 2020; Foitzik et al., 2018; Yan et al., 2021). For instance, asphalt surfaces cause 1.4 to 2 times less tire wear than concrete surfaces in Arizona, USA (Pant and Harrison, 2013).

Only 1% of tire wear is released as PM10 (Fussel et al., 2022). Laboratory experiments have shown that tire wear particles can vary greatly in size, ranging from below 100 nm to above 30 µm (Zhong et al., 2024). Dahl et al. (2006) found that the mean diameter for tire wear particles (by number) was 15-50 nm, with an emission factor of 3.7×10^{11} particles/veh/km at an initial braking speed of 50 km/h and 3.2×10^{11} at 70 km/h using a vehicle turbulence-induced road simulator. Another laboratory-based study using an Engine Exhaust Particle Sizer (EEPS) installed between the tire and road surface found particles ranging from 6 to 562 nm, with the maximum appearing at 30-60 nm [Mathissen et al., 2011]. Kwak et al. (2014) conducted both road experiments and laboratory simulations and found the peak diameter to be 60 µm in road experiments and 30-40 nm in laboratory experiments. However, Camatini et al. (2001) concluded that tire wear particles could reach several hundred micrometers using electron microscopy in an automotive testing facility.

Not all tire wear particles become airborne. Tire shreds may be deposited directly onto the road surface, and some of the coarser airborne material may quickly settle out due to gravity [Thorpe and Harrison, 2008]. This is supported by Fausers et al. (2020), who indicated that most tire wear particles generated by tire-road friction settle on the road, and only 5% of the total suspended particulate matter in cities comes from particles that enter the air directly or through resuspension. Tire rubber develops an electrostatic charge, causing a fraction of the particles to adhere to the vehicle's surface, complicating data collection for tire emission studies [Hildemann et al., 1991; Roggee et al., 1993; Thorpe and Harrison, 2008]. The average tread wear for tires is reported to be between 6 and 9 mg/km, depending on road, tire, and vehicle conditions [Pant and Harrison, 2013].

These studies show significant differences in tire wear particle sizes, highlighting the variability and complexity of tire wear emissions.

1.2.3: Resuspension of Road Dust

Road dust consists of coarse-sized particles derived from various sources, such as industrial emissions, mineralogical dust, and construction emissions [Pant and Harrison, 2013]. The composition of road dust exhibits spatial and temporal variations, making it challenging to classify dust into crustal, re-suspended, or directly emitted [Pant and Harrison, 2013]. Road surfaces serve as locations where particles from a wide variety of sources are deposited. The amount of re-suspended road dust particles depends on a number of factors such as vehicle movement (particularly traffic speed), street maintenance, season and associated meteorological parameters and vehicle speed [Pant and Harrison, 2013]. A fraction of the PM resulting from abrasion processes will be sufficiently large to settle out under gravity and deposit on the road surface [Thorpe et al., 2007]. Exhaust particles, de-icing salt and grit, biogenic and geogenic material may all be carried from nearby locations and deposited on the road. Virtually any anthropogenic and natural resources may result in the deposition of PM on the road. Thorpe et al. (2007) reported a strong association between heavy-duty vehicles and resuspension in the UK, with wind speed not being a significant influence. Furthermore, precipitation was found to have no influence on the amount of resuspension [Pant and Harrison, 2013]. In a related study in Spain, street washing was reported as being ineffective for a PM control-based experiment. Yet in Sweden, road wetness was found to be an important factor as to the amount of re-suspension that occurred but there was a much greater amount of PM due to road sanding and the use of studded tires in Sweden [Pant and Harrison, 2013]. This is because with road studded tires, there is a high amount of road abrasion which occurs. During the wintertime the snow and ice (moisture) keep the roads wet, thus lessening the suspension of particles. In early spring evaporation rates increase due to solar radiation and higher temperatures, making roads dry up more efficiently, thus increasing in road dust resuspension [Omstedt et al., 2005]. In the USA, road dust resuspension is responsible for 65% and 79% of fine and coarse emissions [Matthaios et al., 2022]. The issue with identifying non-exhaust emissions from road dust emissions is complicated due to the interaction with deposition. Road dust particles may settle onto the road surface, making identification of emissions from road surface wear far more complex. Road surface dust may have much in common compositionally with local crustal materials, but only through carefully controlled field experiments can these complexities be detangled [Pant and Harrison, 2013].

A review of non-exhaust emissions conducted in 2018, which reviewed 256 source apportionment studies, found that 71% of the studies showed road dust as the main contributor of non-exhaust emissions, and 8% and 9% of these studies showed brake and tire wear contributions, respectively. Additionally, 12% of them reported an external source of non-exhaust emissions [Matthaios et al., 2022].

1.3: Exhaust Emissions

Exhaust emissions are an important source of carbonaceous aerosols, particularly in the fine size range. A carbonaceous aerosol is a carbon-containing compound that forms during the combustion process within an engine and is then released into the atmosphere, such as soot [J.H.Seinfeld, 2015]. Emissions from vehicles depend on the engine type, age, maintenance, and include elemental and organic carbon with various trace elements associated with incomplete combustion of fuel and oil additives [Matthaios et al., 2022]. The primary emissions are formed in the engine and exhausted from the tailpipe which are formed in the engine, typically ranging from 30- 500 nm [Conte and Contini, 2019]. The secondary exhaust emissions are due to condensation in the diluting exhaust plume and are sized below 30nm [Conte and Contini, 2019]. Exhaust emissions of PM from road vehicles have gradually been reduced due to the new technologies and stricter legislative limits [Matthaios et al., 2022].

1.4 Key flow and mixing features in an urban area

An urban area has street canyons where the concentration of pollutants can be several times higher than in locations with unobstructed land. This variance depends on traffic characteristics, street canyon geometry, entrainment of emissions from adjacent streets, and turbulence-induced prevailing winds [Kumar et al., 2011]. Traffic emissions in urban areas generally take place within the urban canopy layer, where atmospheric flow is heavily disturbed by buildings and obstacles (Figure 3). This disturbance leads to varying flow and dispersion characteristics of pollutants in different urban settings, influencing the dilution of these emissions. When considering nanoparticles and their dynamics for dispersion modeling, dilution remains a crucial process [Kumar et al., 2011]. Additionally, dilution is accompanied by transformation processes such as nucleation, coagulation, condensation, evaporation, and deposition. The occurrence of these processes, just after the release of emissions from vehicle tailpipes into the atmosphere, continuously alters the number and size distribution of nanoparticles. This dynamic nature makes dispersion modeling challenging and distinct from that for gaseous air pollutants.

The flow of wind and/or the mixing of pollutants through or above urban areas is not straightforward. This complexity arises due to the intricate network of streets and buildings, synoptic scale winds, surface heating, and various pollution sources such as moving traffic [Kumar et al., 2011]. Understanding turbulent mixing mechanisms, such as vehicle-induced turbulence, road-induced turbulence, and atmospheric boundary layer turbulence, has improved predictions of the spatial gradients of air pollutants near roadways [Kumar et al., 2011]. A straightforward approach to describing urban scales is as follows: street length scale (less than ~100-200m), neighborhood (up to 1 or 2km), city (up to 10 or 20 km), and regional (up to 100 or 200 km) scales [Kumar et al., 2011]. The smallest length scale is that of the vehicle wake, where the mixing and dilution of pollutants occur faster than at any other scale. For the purpose of this study, the largest impacts come from the vehicle wake and street canyon length scale; however, there are larger impacts that can be attributed from neighbourhood and city scales.

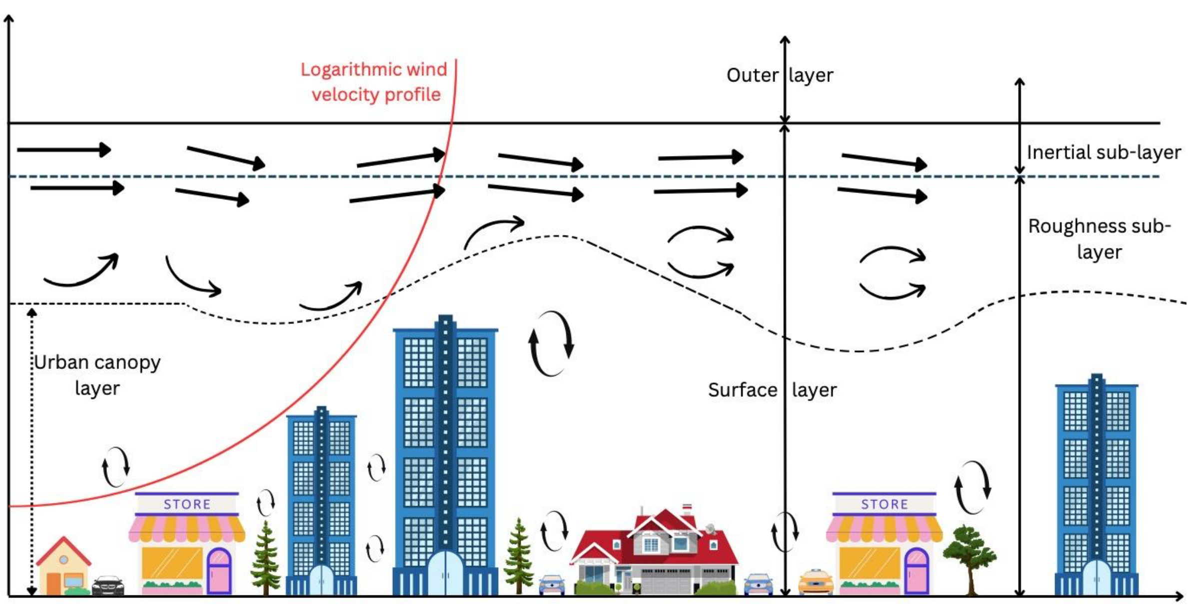

Figure 3: Schematic diagram of flow through and over an urban area as well as various layers in the ABL and horizontally spatially averaged mean velocity profile based on schematic presented by Kumar et.al.,2011.

1.4.1 Vehicle Wake

The vehicle wake plays a crucial role as the initial spatial scale for the dispersion of emitted nanoparticles into the ambient environment. The extent of particle transformation is contingent upon flow characteristics, with turbulent mixing governing dilution and background concentrations. According to Kumar et al. (2011), the vehicle wake is comprised of two regions: a) the near wake, generally considered up to a distance of about 10-15 times the vehicle height, and b) the far or main wake, a region beyond the near wake (Figure 4). Rapid changes in the number and size distributions of nanoparticles occur in the near wake due to various transformation processes encouraged by swift turbulent mixing and dilution. Zhang and Wexler (2004), as cited by Kumar et al. (2011), reported a dilution ratio of up to 1000:1 within 1-3 seconds after the release of emissions, while Kittelson (1998) found a similar dilution ratio occurring at 1-2 seconds in the near wake.

In the process of diluting and cooling exhaust, new particles form through homogeneous nucleation and immediately grow via the condensation of condensable vapors [Kumar et al., 2011]. The high number concentration of newly formed particles leads to immediate coagulation, thereby transforming the particle size distribution. According to an on-road measurement study cited by Kumar et al. (2011), the nucleation mode was already formed after a residence time of 0.7 seconds in the atmosphere. Many modelers use these size distributions as initial emission size distributions. In the far wake region, the rate of evolution is much slower because vehicle-produced turbulence decays with increasing distance from the tailpipe, and mixing is primarily dominated by atmospheric turbulence [Kumar et al., 2011]. The particle processes, which include but are not limited to, nucleation, coagulation, condensation, evaporation, and also deposition, may last up to tens of seconds, depending on the atmospheric conditions and urban setting. On a short time scale, coagulation of particles above 10 nm is too slow to substantially affect the number concentration.

1.4.2 Street Canyon

The emitted parcel, whether exhaust or non-exhaust, further disperses within the street canyon. The flow direction is influenced by various factors: i) geometry and aspect ratio (average building height, width, and ratio) categorizing into regular, deep, avenue, and symmetric canyons, ii) urban roughness elements within the canyon (trees, balconies, slanted roofs, etc.), iii) street orientation, and iv) synoptic wind conditions [Kumar et al., 2011]. Depending on the free-stream velocity or the wind speed above the roof (U), the flow can be neutral ($U < 1.5$m/s, atmospheric stability is neutral), perpendicular or near perpendicular ($U >$ 1.5m/s, blowing at an angle of more than 30° to the street axis), and parallel or near parallel ($U >$ 1.5 m/s, blowing from all other directions) [Kumar et al., 2011].

In the case of regular street canyons, the typical recirculating velocities are approximately 0.33-0.5U, and the turbulence levels are about 0.10U [Kumar et al., 2011]. The mixing of the parcel within a canyon depends on the ventilation flux of air from street canyon turbulence produced by the wind and atmospheric stability [Kumar et al., 2011]. The shape and strength of the wind vortices may also be influenced by atmospheric stability and other thermal effects induced by the walls and/or the road [Kumar et al., 2011]. Wind and traffic-induced turbulence are generally considered the main mixing mechanisms at this scale [Kumar et al., 2011]. During calm wind conditions, the mixing of the parcel will be dominated by traffic-induced turbulence and atmospheric stability conditions, while wind-induced turbulence will prevail during larger wind speeds [Kumar et al., 2011]. The magnitude of mechanical mixing increases with the rise in wind speed and surface roughness. Solar radiation heating the building walls in a street canyon might generate an upward buoyancy force. However, laboratory, computational, and previous field studies show only a small effect, which is unlikely to be operationally significant in most scenarios [Kumar et al., 2011]. This is because the physical width of the free convective boundary layer on the heated wall is small compared with the scale of the mechanically driven motion [Kumar et al., 2011].

Urban Scale	Key Flow and Mixing Features
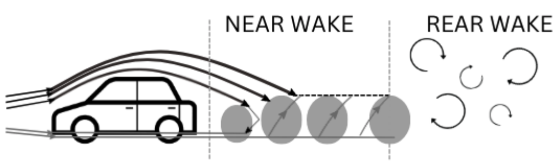	• Flow is more turbulent in near wake than far wake region • Traffic induced turbulence is intense in near wake and dominate the mixing • Atmospheric turbulence leads to the further mixing in far wake region
	• Surface roughness below building height influences flow features and mixing. • Mixing layers within or above the building are comparable to the building or street dimensions. • Mixing due to traffic takes precedence over wind-induced mixing in calm wind conditions. • Thermal turbulence, generated during hot sunny weather and light winds, may contribute to mixing.

Figure 4: Description of flow and mixing characteristic at various urban scale based on schematic provided by Kumar et.al., 2011.

1.5 The Use of The Eddy Covariance to Measure Emissions

Vertical fluxes are observed as a result of the turbulent transport of emissions measured at the site, which can originate from any point. Measuring turbulent flux in a city is particularly challenging due to the inhomogeneous terrain, making it more difficult compared to rural areas. The eddy covariance (EC) method is the most direct method for measuring the exchange between the surface and the atmosphere. The essence of the EC method lies in its ability to compute vertical flux by correlating aerosol concentration and vertical velocities. This process enables the estimation of traffic-related particle pollution strength, taking into account the influencing surface area.

For accurate EC measurements, it is recommended that the surface flux be measured in the inertial sublayer and be free from obstructions (Roth, M., 2000). This assumption is easily met in rural settings but becomes more challenging in urban environments due to non-homogeneous terrain. In urban areas, EC measurements are often conducted on top of buildings or other high-standing structures, such as telecommunication towers (Ao et al., 2016; Brümmer et al., 2013; Keogh et al., 2012; Liu et al., 2012; Nordbo et al., 2013; Wood et al., 2010; Järvi et al., 2018). This approach minimizes the effects of the structure itself on the EC measurements. However, these measurements are not completely free from the impact of roughness elements, even if the measurement height is sufficiently above the surrounding roughness elements (Järvi et al., 2018).

Despite this setup, obtaining high-quality EC data can still be challenging due to the effect of flow distortion caused by the interaction between the building or measurement platform and the collection method (Barlow et al., 2011). Many studies have implemented the method of calculating EC on top of buildings, including Conte and Contini (2019).

This review examines the findings of Conte and Contini (2019), who determined emission factors (EFs) for vehicular particles across different size ranges. Their methodology involved the EC technique to measure vertical turbulent fluxes and concurrent vehicle traffic rate analysis.

The research was conducted in Lecce, Italy from the 10^{th} of March to 24^{th} of April, 2015. The experimental sites were located approximately 14 m above the road level and utilized a suite of instruments to collect EC measurements, including an ultrasonic anemometer, a thermohygrometer, a Condensation Particle Counter (CPC), and an Optical Particle Counter (OPC). A secondary set of instrumentation was implemented, which included a PC with a specific software and pump, to maintain a turbulent flow rate in the inlet tubes. Furthermore, two network video cameras, facing each side of the road, were implemented with a motion detection software to count vehicles passing on the main road. The motion detection software counts the number of vehicles moving along the road from both directions. To test the accuracy of the automatic counting, the results of the software were compared with manual counting in specific periods, and it was found that the uncertainty of the automatic evaluation of the traffic rate was 12%. The measurement station was located at the corner of the roof and the anemometer was placed on a boom extending 1 m outside the perimeter of the roof to limit the influence of the building on the flux measurements.

The implementation of a footprint flux model aids in providing additional spatial context to the flux measurements, including spatial representation and quantitative analysis. The footprint model is represented as the following equation:

$$F(z_m) = \iint_0^{\infty} S\,(x, y, 0) f(x, y, 0) dx\, dy' \qquad (1)$$

Where F is representative of vertical turbulent flux, measured at some height above the ground, z_m in the stream-wise x direction. $S\,(x, y, 0)$ is the spatial distribution of surface fluxes that is the source strength of the substances, with x and y indicating the streamwise and crosswind directions. With $f(x,y,0)$ is the spatial distribution of the footprint. The footprint model determines the source area that contributes to the flux measurements taken, which allows for quantitative assessment of how much different areas contribute to the measurements. With a footprint analysis, the source area can be integrated over the exact length of the road in order to determine the emission rate. The crosswind-integrated footprint is estimated using a Lagrangian stochastic dispersion or analytical model. In order to represent data that corresponded to the direction perpendicular to the road the dataset was filtered such that the wind direction is from 292.5º ± 10º and windspeed > 0.6 m/s, to avoid calm conditions. The footprints were evaluated using the complete set of 30-min period measurements with the integration's points being x_1=23 and x_2= 45 m, where the main road is located. The average footprint value within the range of the road was found to be 0.005m^{-1}. This value helps to understand the spatial impacts of the road emissions on the air quality. The average footprint value of 0.005 m^{-1} within the road's range indicates that each additional meter from the road corresponds to a decrease in the road's emission influence by a factor of 0.005.

The traffic rate for the road was within a range of 380 vehicles per hour (vehicles/h) to 1890 vehicle/h. The measured fluxes were highly correlated with the traffic rate and this supported the hypothesis that the vehicular traffic from the main road was the dominant particle source. During the research period positive upward aerosol fluxes were dominant even though deposition cases were present, mainly for large particles and when the traffic rate was low. Negative fluxes, which represent deposition, for relatively large particles were also observed in other urban areas and they could be due to different dynamics of coarse particles and/or influence from traffic sources located at larger distances from the measurement site. If the net flux is negative in a specific 30-min interval, this implies that deposition is dominant compared to the emissions and thus the corresponding measurements cannot be used to investigate vehicle emissions [Conte and Contini, 2019].

The study found that particle number emission factors are dominated by ultrafine particles (particle size < 250 nm), with the exhaust emissions having the average value of 2.2×10^{14} per vehicle km driven (#/vehicle km) with a $\pm 6.3 \times 10^{13}$, 95% confidence interval. Moreover, the EFs are representative of the entire vehicle fleet and due to the limited number of data points available for the footprint evaluation, the EF should be considered as "estimates" and treated appropriately [Conte and Contini, 2019]. Calculating the EF allows for quantification of the traffic-related particle strength. An emission factor attempts to relate how much of a pollutant is released into the atmosphere with respect to the traffic rate. The EF is evaluated by considering the particle exchange between the surface and the atmosphere, enabling comparisons with results from previously published studies. The formula used is:

$$EF = \left. \frac{Flux}{Footprint} \middle/ Traffic\ Rate \right.$$

EF mass size distribution shows a first maximum at 300 nm and a successive decrease up to approximately 900nm. The decrease was found to be extremely steep for particles up to 900 nm with a reduction by four orders of a magnitude (Figure 4). For particles with a diameter > 900 nm there is an increase of EF likely due to the increase of the contribution of non-exhaust emissions. It was assumed that the high presence of the traffic lights causing frequent stop-and-go and acceleration after traffic lights might contribute to the high value of small particle emissions. The mixed vehicle fleet EFs evaluated in this work compared well with the other works performed in urban areas under real operating conditions for both number and mass. However, comparing the total number of particle emission factors difficult, mainly due to the different size ranges of the instruments used. This is because nanoparticles dominate emissions and a small change in the size range of the analysis could produce wide changes in the evaluated EFs. The comparison of the total number of emission factors obtained in 2010 and in 2015 in the

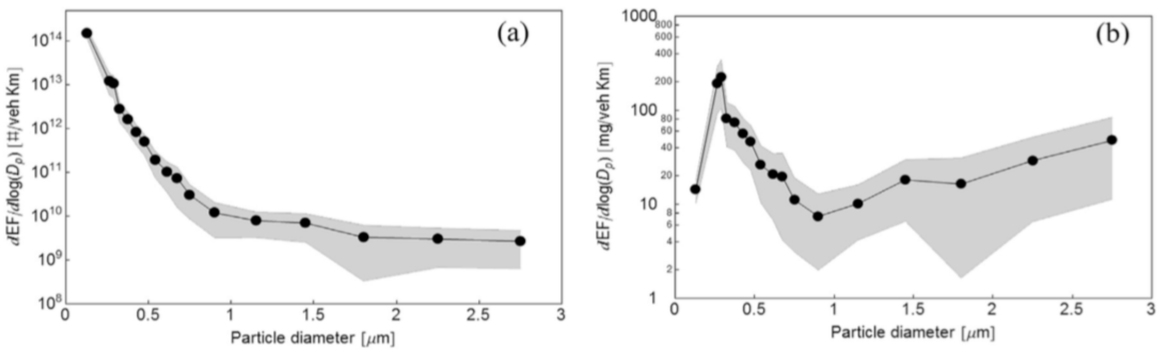

Figure 5: Average size resolved particle emission factors for the mixed vehicle in (a) and mass (b). The grey shaded region is the 95% confidence interval. Conte and Contini., 2019

same urban area found a 56% decrease in the EFs from 2015 possibly due to the increased use of new generation passenger cars that have more restrictive European limits for particle emission.

1.6: Measuring Ultra-fine Particles from Vehicular Emission

This study was conducted during a phase of the COVID-19 lockdown, in January 2021, when schools and most workplaces were closed, significantly affecting daily routines and reducing vehicular traffic in Toronto. Traffic volume decreased by 52% during the morning peak (8-9 a.m.) and 68% during the evening peak (5-6 p.m.) ["City of Toronto Traffic Data Shows More People Staying Home to Fight Covid-19.", 2021]. Donateo et al. (2021) analyzed the effects of these restrictions, in Italy, on ultrafine particle (30nm to 1000nm) number concentration and turbulent fluxes in a suburban area.

The Donateo et al. (2021) study was conducted 3.5km southwest of the town of Lecce, Italy, April 2016 to November of 2020, in which the baseline values for normal traffic conditions were determined using the data collected from 2016- 2019. The experimental sites were located approximately 20 m above the road level to measure vertical fluxes to which the eddy covariance method was applied. A suite of instruments was used to collect EC measurements, including an ultrasonic anemometer, a thermohygrometer, and a Condensation Particle Counter (CPC). The study found that the lockdown led to a significant reduction in the ultrafine particles, with a drop of 64% in particle number concentration during the lockdown. In contrast, larger particles such as $PM_{2.5}$ and PM_{10} saw a smaller reduction of 14%. The ratio of $PM_{2.5}$ to PM_{10} remained constant at 0.54, suggesting no change in particle size distribution. Furthermore, there was a 30% decrease in the number size distribution of particles during this period, which likely reflects reduced traffic activity.

Analysis of ultrafine turbulent fluxes revealed a shift from the site being a source of particles to a sink. From 2016 to 2019, 61.9% of fluxes were positive (emission) and 31.1% negative (deposition) During the lockdown, positive fluxes decreased by 61%, and negative fluxes by 59%. This reduction was more pronounced in emission fluxes than in deposition fluxes. This change was more pronounced in emissions than deposition. Daily anomalies calculated during the lockdown showed predominately negative values, with a mean daily anomaly of -4223 particles cm^2/s for positive fluxes and -2432 particles cm^2/s for negative fluxes. Pre-lockdown anomalies were positive but turned negative post-lockdown, indicating the site acted more as a sink for ultrafine particles.

Straaten et al. (2022) conducted a similar study in Berlin, Germany which also implemented eddy covariance measurements of size-resolved of sized resolved particle numbers to investigate the effect the reduced traffic intensity on particle flux. This study found a 38% reduction in median ultrafine particle fluxes during the lockdown, directly correlating with a

35% traffic reduction. Unlike Lecce, the Berlin site remained a net positive particle source, with a slight increase in deposition (+3.2%) during the lockdown. This discrepancy is likely due to the different levels of baseline traffic: Lecce being a smaller town with fewer vehicles, and the Berlin site being located next to a main road with an average vehicle intensity of 47,000 vehicles per day.

These studies demonstrate that the relationship between vehicular traffic and particle fluxes is not straightforward; significantly reduced vehicle numbers can inversely affect flux behaviors. This indicates that a road being a source of particles due to high traffic may not always hold true under varying traffic conditions.

1.7: Comparative Analysis of Emission Factors in Urban Vehicle Fleets: A Canada-Italy Perspective

Building upon the work conducted in Conte and Contini., 2019 our study seeks to answer a similar question regarding the change in emission factors of emissions in an urban city. The study described herein uses different instrumentations compared to Conte and Contini (2019), as which outlined in Chapter 2: Methodology. Since this study is conducted in Canada the fleet type differs slightly compared to the study conducted in Italy. As of 2021, Ontario, Canada had an average of 78% gasoline-based and 13% flex fuel [Hayley Vesh, 2021]. Flex fuel, formally known as E85, contains 85% ethanol and 15% gasoline, which is a renewable fuel source [Hayley Vesh, 2021]. The remaining vehicles included diesel, electric vehicles (EV), and unaccounted for vehicle types [Hayley Vesh, 2021]. Italy, during the research campaign in 2015, comprised a vehicle fleet which had 55.2% diesel vehicles, 31.4% gasoline, with the remaining comprising of hybrid EVs and flex fuels ["Trends in Fuel Type of New Cars between 2015 and 2016, by Country", 2021]. From 2015 to 2021, EV use in Italy grew by 0.09% to 4.6%, [Mathilde Carlier, 2023] while Canada saw a growth of 3.7% of EV car sales between 2015 and

2021 [Klippenstein, M., 2016; Carlier. M., 2023]. With a similar increase of EV sales in both region there is expected to be a drop in average emission factor. However, with COVID-19 lockdowns across southern Ontario in 2021, the results may be further skewed as fewer cars were on the road than they would have been during 2015.

Chapter 2: Methodology

2.1: Experiment Site Setup

The study was conducted on Dufferin Street Toronto, Ontario, Canada at the Fairbank Memorial Community Center (Figure 6a), located at 43.69134°, -79.44805°. The experimental instruments were placed on the roof of the recreation center building at the roof height of 7.0m above the road level. The measurements were taken from December 21, 2020, to May 22, 2021. The study area is mostly residential and there is a high density of buildings surrounding the recreation center. There are two-storey buildings on each side of the street, creating a street canyon. The main mixing mechanism in this system is wind and traffic turbulence with little influence from vegetation or the urban canopy. The measurement station was situated at the corner atop the roof of the recreation center (Figure 6b), facing Dufferin Street. The instrumentation and supporting equipment included a sonic anemometer (Applied Technologies Vx Probe) (Figure 5b), a laptop to collect the data from the sonic anemometer, an Ultra-High Sensitivity Aerosol Spectrometer (UHSAS) (Droplet Measurement Technologies UHSAS-G) (Figure 3), and a security camera to record video footage.

The Applied Technologies Vx Probe sonic anemometer measured the high-frequency wind speed from three spatial vectors as well as temperature, the anemometer here is used to determine turbulence measurements. The sonic anemometer used in this setup operated at a frequency of 10Hz, with a wind speed accuracy of ± 0.01 m/s and sonic temperature accuracy ±1.00ºC [“Ultrasonic Anemometer Probe Styles”,]. The anemometer boom extends past the roof's perimeter by only 20cm, leaving room for influence from the building in the flux measurements.

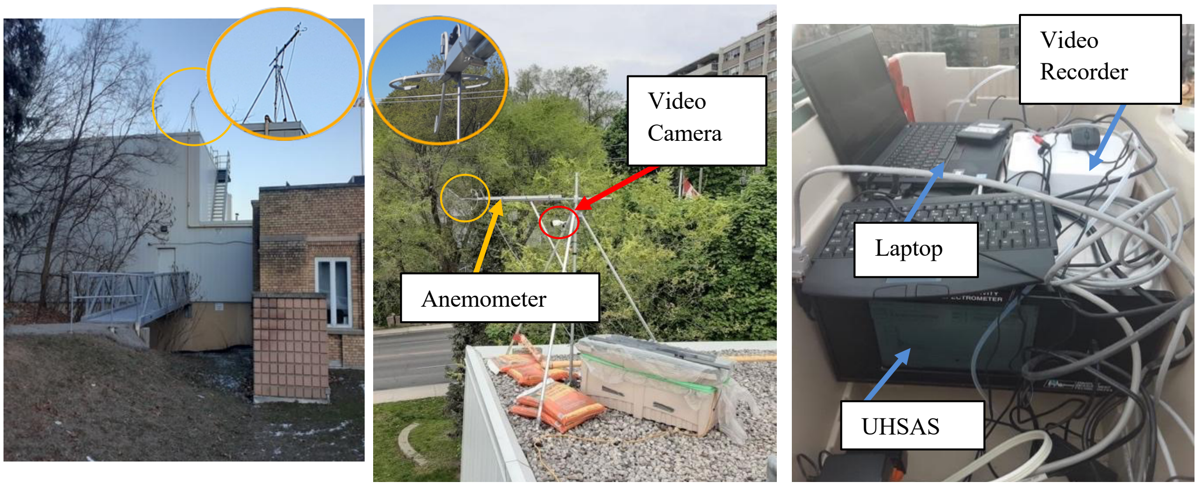

Figure 6: a) Ground view of the research site. Area circled in orange represent the station. b) The instrument setup from atop the roof. The security camera is circled in red into to see it more clearly c) Placement of the instrumentation setup within the tote.

The Ultra-High Sensitivity Aerosol Spectrometer (UHSAS) is a laser-based spectrometer system that uses optical scattering for sizing particles ranging from 60 nm to 1000 nm. Size-resolved diameters were measured at a frequency of 1Hz, and each sample is stored as a histogram consisting of 99 standard size bins (Figure 6). The UHSAS measures the aerosol scattering signature produced by illuminating each particle with a 1054 nm laser (1 kW of power). It estimates the particle diameter from a calibration curve (which assumes spherical particles). A pump and tubing system is used to draw air from the entrance of the tubing main line co-located near the anemometer to the UHSAS**.** The pump takes in air through an inlet co-located with the anemometer.

The UHSAS sub-samples from this pump line held constant at 49 sccm ±1 sccm [Ultra High Sensitivity Aerosol Spectrometer (UHSAS), 2017]. The UHSAS sampled from a stainless-steel main line (inner diameter = 4.2 mm, outer diameter = 6.2 mm, length= 2.6 m) at a tee junction to the pump which was then connected to a plastic line connected to the UHSAS (inner diameter= 1.7 mm, length =1 m). The entrance of the steel main line had a rain cover, approximately 2.54 cm in diameter to keep sampling as uniform as possible with limited external factors. The travel time between the main line and the pump is 0.2 seconds, and from the pump to the UHSAS is approximately 1.4 seconds, making the residence time just less than 2 seconds [Miller, S., 2022]. With the residence time of particle within the inlet, diffusion and sedimentation may cause particles to deposit on the walls of the tube, resulting in a particle loss of 4 to 11%, especially particles with diameters < 100nm and > 700 nm [Miller, S., 2022, Miller et al., 2019].

The UHSAS is known to have limitations that may affect its measurements and lower its detection limits. Miller (2022) investigated the performance of the UHSAS used in this study by comparing its results to a condensation particle counter (CPC) for total number concentration and to a differential mobility particle sizer (DMPS) for ammonium sulfate and polystyrene latex particle diameters. For ammonium sulfate particles ranging from 200 to 500 nm, the UHSAS underpredicted the total number concentration by up to 24% compared to the CPC, with the largest discrepancies found for the highest particle concentrations (Miller, S., 2022). The diameter of ammonium sulfate particles measured by the UHSAS aligns well with DMPS measurements for particle diameters below 200 nm, but the UHSAS underestimates the diameter in an almost linear fashion as it increases toward 500 nm. At 500 nm, the UHSAS measured ammonium sulfate particle diameter is about 15% lower than that measured by the DMPS. For polystyrene latex particles, the UHSAS measurements agree with those of the DMPS. Similarly, Willis et al. (2019) found that the UHSAS underestimates particle volume between 250 nm to 500 nm by approximately 20%. Additionally, the UHSAS assumes particles are spherical when measuring their diameter; however, in reality, particles vary in shape and density. For example, a cylindrical-shaped particle could be recorded as having a size of 500 nm if oriented in a certain way as it enters the UHSAS.

For the period from December 21, 2020 to January 12, 2021 the UHSAS frequency was of 0.33 Hz, collecting information every 3 seconds instead of the standard 1Hz. The frequency of 0.33 Hz is too slow to accurately calculate flux measurements as it is unable to capture the rapid fluctuations in wind speed and direction that can occur over shorter time periods.

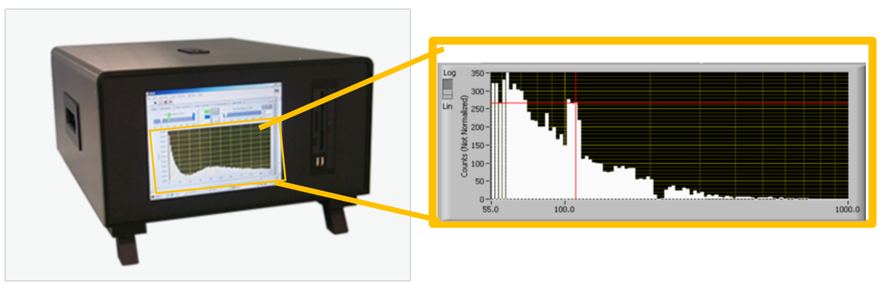

Figure 7: The UHSAS and a magnified image of operation screen which shows the histogram of the amount of emission for each diameter size per second, which would be recorded into the 99 bins.

Figure 8a shows the height of the station, where the bottom section, at the bottom end of the measurement block, is at the same elevation as the road. The anemometer was positioned such that its perpendicular distance to the nearest boundary of the road is approximately 31.3 meters, and to the furthest boundary is about 47.1 meters (refer to Figure 8b). Therefore, the source area of emissions is between 31 m and 47 m, which becomes the integration range for the footprint flux. The wind direction plays a critical role for the data collection since it influences the transport of emissions towards the receptor. The wind direction must be from the southwest quadrant as this would ensure the wind flows directly across the road towards the anemometer. Otherwise, if the wind from another direction, the calculated flux would not have originated from the area under investigation. Moreover, wind speeds play a critical role in the movement of emissions. Low wind speed cause uneven mixing and weak eddies causing emissions to remain near the ground, resulting in the deposition of particles on the road. On the other hand, with strong winds, the air can bring the emissions upwards due to the turbulent exchange.

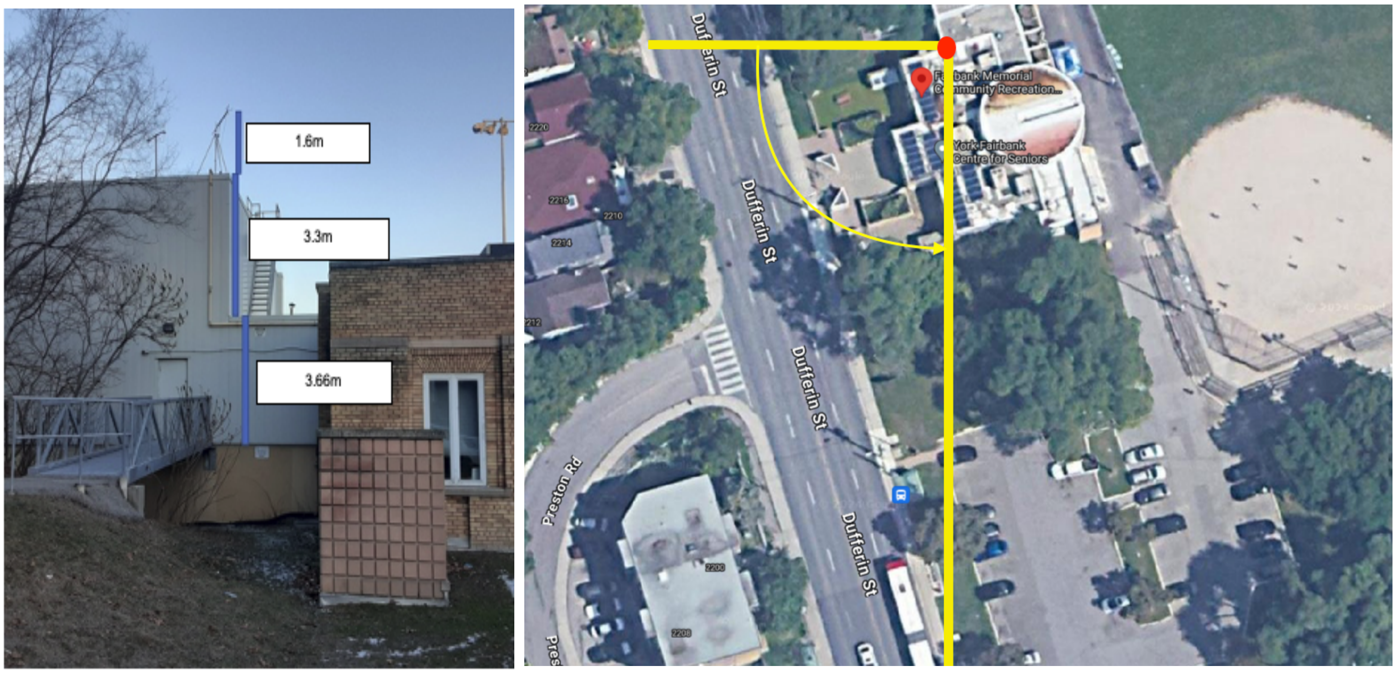

Figure 8: a) The height of the building from ground level. b) The aerial view of the experimental site showing the wide range of wind directions which account for the between "from the road" emissions. This is the range of180 degree and 270 degrees.

2.2: Rotation Correction

Small errors in the alignment of turbulent wind sensors can result in large errors in the measurement of momentum fluxes. This is due to cross contamination of velocities that can occur in a tilted sensor, where the fluctuations in the longitudinal component of wind appear as vertical velocity fluctuation and vice versa [Wilczak et al., 2000]. Typically, sonic anemometers are mounted on a horizontal boom, similar to our setup, and the sonic boom drops slightly below horizontal as it extends outwards ["Sonic Tilt Corrections."]. Since the anemometer is stationed on a building over sloping terrain, fluctuations in the streamwise velocity can create large apparent stresses that are a function of the slope angle relative to the wind direction. This makes it difficult to compare turbulence measurements taken over a slope to a flat terrain [Wilczak et al., 2000]. The tilt correction is necessary to rotate the sonic anemometer toward the streamwise coordinate system, which aligns it with the mean wind direction, removing lateral shear stresses and leveling the anemometer to the ground. The first rotation is around the z-axis to make $\overline{v_1} = 0$, creating new velocity components given in Equation 2a. The measured wind components are represented by the subscripts *m* and the new velocity components, after the first rotation, are represented by subscript 1. θ is used to determine the wind direction which is later used to filter time periods when the wind direction is between 180° and 270° corresponding to the wind flow perpendicular to the road and directly in line with the anemometer. The second rotation is around the y-axis until the $\bar{v} = 0$ so that the x-axis points in the mean steamline. The following equations represent how the first rotation (2a) and second rotation (2b) are calculated:

$$\begin{aligned} u_1 &= u_m cos\theta + v_m sin\theta \\ v_1 &= -u_m sin\theta + v_m cos\theta \\ w_1 &= w_m \end{aligned} \qquad (2a)$$

Where, $\theta = tan^{-1}\frac{\bar{v}_m}{\bar{u}_m}$

$$\begin{aligned} u_2 &= u_1 cos\phi + w_1 sin\phi \\ v_2 &= v_1 \\ w_2 &= -u_1 sin\phi + w_1 cos\phi \end{aligned} \qquad (2b)$$

Where, $\phi = tan^{-1}\frac{\bar{w}_1}{\bar{u}_1}$

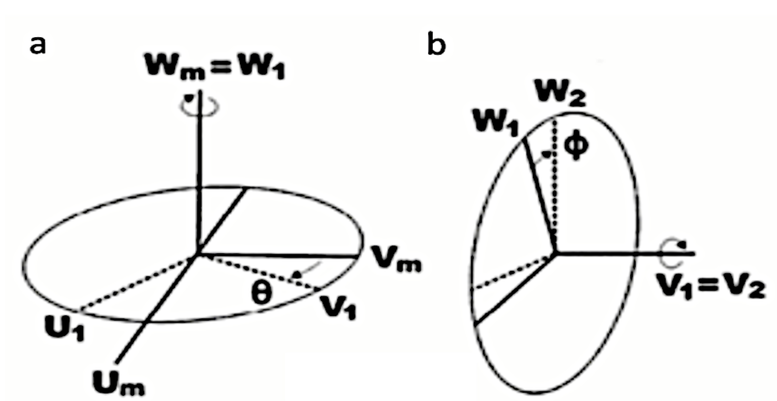

Figure 9: Definition of the coordinate rotation. a) The first rotation corresponding to equations 2a. b) The second rotation corresponding to equation 2b [Foken, 2008].

2.3: Flux and Footprint

The eddy flux covariance was used to calculate vertical turbulent fluxes within the atmospheric boundary layer. The vertical flux represents the turbulent transport of aerosols per unit time and per unit area making it useful to quantify vehicle emission rates from the traffic. The turbulent vertical flux of aerosols is calculated as:

$$F = \overline{\mathrm{w'N'}}, \tag{3}$$

where $w_2{}'$ is the perturbed vertical wind speed (after rotation) and N' is the particles per volume which is a derived from $N = \bar{N} + N'$. *N* is calculated as:

$$N = \frac{C}{F_V} \tag{4}$$

where *C* is particles per second, F_V is sample rate and *N* is particle per volume, averaged over 30-minute periods.

A footprint flux is a mathematical way to understand how much a specific area on the ground contributes to the vertical turbulent flux measurements taken at a sensor placed at some height. It links what is happening on the ground (such as the release of emissions) to what is being measured. The footprint flux is related to source contribution as it acts as a transfer function to connect the source or sink, in this case, of emissions, at ground level to the turbulent flux measured at the height of a sensor. To estimate the position and size of the source areas and the relative contribution of passive scalar sources to measure flux, flux footprint models integrate over the location of interest, in this case, the length of the road [Kljun et al., 2015]. Long term and short-term flux observations require extensive footprint calculations as they are exposed to widely varying atmospheric conditions, making understanding difficult. Even with the widespread use of the footprint models, the selection of a suitable model still poses major challenges. Footprint models can be based on large-eddy simulation, Eulerian models, Lagrangian stochastic particle dispersion, or a combination of Large Eddy Simulation (LES) and Lagrangian particle dispersion (LPD), which can resolve complex flow structure (e.g. flow over a forest edge or a street canyon) and surface heterogeneity [Kljun et al., 2015]. However, these methods are labour intensive, and thus cannot be used in long term practice, as they are best for cases studied over selected hours or days and most are constrained to a narrow range of atmospheric conditions. These complex models are not suited for dealing with long-term flux measurements, which is the case for this study. Thus, a computationally inexpensive footprint model is needed that can deal with months' worth of half-hourly data points. Analytical footprint models provide a compromise with regards to simplicity and speed; however their validity is often constrained to ranges of receptor heights and boundary layer conditions [Kljun et al., 2015]. Older footprint models, such as the Horst and Weil footprint model, offered simple parameterizations with limitation to a particular turbulence scaling domain (often surface layer scaling), or a limited range of stratifications [Kljun et al., 2015]. In 2004, Kljun introduced a footprint parameterisation based on a fit-to-scale footprint estimate derived from a Lagrangian stochastic particle dispersion model, hereafter referred to as LPDM-B, which is a footprint model valid for a wide range of boundary layer stratification and receptor heights. However, like the older footprint models it was still a one-dimensional model comprising only the crosswind-integrated footprint to an upwind extent, but not its width [Kljun et al., 2015].

The footprint analysis used for this work was a two-dimensional Flux Footprint Prediction (FFP), derived by Kljun et al. (2015), which provides not only the extent but also the width and shape of footprint estimates. The FFP model is an improvement over the LPDM-B, as it is better suited for elevated measurements in stable stratification. The model incorporates surface roughness into the scaling approach, and more importantly, this model implements the crosswind spread of the footprint, being useful as the source can be observed not just from the *x* - axis but also the *y*- axis. This allows for the investigation of the footprint flux within the integration zone of the road in the *x*- axis (31 m to 47 m), upwind from station, as well as spread of emission source across the road in the y-axis, especially for periods of congestion downwind when vehicles come to a stop.

The footprint is strongly dependent on the receptor height, z_m, which is the first parameter [Kljun et al., 2015]. The footprint function links what is happening on the ground (such as the release of emission) to what is being measured up at the receptor height.

The mean wind velocity at the measurement height, $\bar{u}(z_m)$, and the surface shear stress, also known as the friction velocity, u_*, directly affect the transfer function in turbulent boundary layer flow [Kljun et al., 2015]. Friction velocity, u_*, is defined as $u_{*0} = [\overline{u'w'}_0{}^2 + \overline{v'w'}_0{}^2]^{1/4}$. This surface layer wind speed profile relates $\bar{u}(z_m)$ to the roughness length, z_0 [Kljun et al., 2015]. A high surface roughness enhances turbulence relative to the mean flow, and thus shortens the footprint [Kljun et al., 2015]. Therefore, non-dimensional upwind distance X^* is first evaluated for the given x:

$$X^* = \frac{x}{z_m}(1 - \frac{z_m}{h})(ln\frac{z_m}{z_0} - \psi_M)^{-1} \quad (5)$$

z_m is the measurement height which is defined as $z_m = z_{station} - z_d$ where $z_{station}$ is the height of the station above the ground, z_d is the zero-plane displacement height, z_0 is the roughness length, and h is the height of the planetary boundary layer height (refer to appendix regarding steps to evaluate the boundary layer height).

All parameters that are denoted with * (except for u_*) represent the non-dimensional form of the parameter. This is because Kljun et al. found using dimensionless scaling makes the model more universally applicable as footprint simulation ran over a board range of scenarios with different atmospheric conditions resulted in a vast range of footprints.

ψ_M is based on the Monin-Obukhov similarity and is the integrated form of the non-dimensional wind shear, which accounts for the effect of stability *(z_m/L)* on the flow and influences the buoyancy on the wind [Kljun et al., 2015]. ψ_M was used as suggested by Garratt, 1992 as:

$$\psi_M = \left\{ -B_1 \frac{z_m}{L} \qquad for\ L > 0 \right\} \tag{6a}$$

$$\psi_M = \left\{ ln(\frac{1+X^2}{2}) + 2ln(\frac{1+X}{2}) - 2tan^{-1}(X) + \frac{\pi}{2}\ \ for\ L\ < 0 \right\} \tag{6b}$$

Where X= $(1\text{-}19\ z_m/L)^{1/4}$, B_1 =5.3 and L is the Obukhov length ($L = \frac{-u^3{}_*\bar{T}}{kg(\overline{w'T'})}$), $\bar{T}$ is the mean potential temperature, k is the von Karman constant, k = 0.4, g is acceleration due to gravity, and $\overline{w'T'}$ is the turbulent flux of sensible heat. X and B_1 are used as recommended by Högström, 1996.

According to Kljun et al. (2015), crosswind dispersion can be described by a Gaussian distribution function with σ_y as the standard deviation of the crosswind distance. The collection of scaled crosswind-integrated footprints $F^{y*}(X*)$ and crosswind dispersion $\hat{\sigma}_y *$ from LPDM-B is consistent enough to be represented by a single fitting function for both the scaled crosswind-integrated footprints and scaled crosswind dispersion. The fitting function for the parameterized crosswind integrated footprints is selected as the product of a power function and an exponential function (Eq 6), and for the scaled crosswind dispersion the fitting function is chosen in conformity with Deardorff and Willis (1975) (Eq 6). By inserting $X*$ into the crosswind - integrated footprint $F^{y*}$and crosswind dispersion σ_y* the fitting function of the parameterized crosswind-integrated footprint $\hat{F}^{y*}$and crosswind dispersion $\hat{\sigma}_y *$ are determined:

$$\hat{F}^{y*} = a(X * -d)^b exp(\frac{-c}{X*-d}) \tag{7}$$

$$\hat{\sigma}_y *= a_c(\frac{b_c(X*)^2}{1+C_cX*})^{1/2} \tag{8}$$

The fitting parameter, *a, b, c,* and *d* are dependent on the constraint that the integral of the footprint parameterisation must equal unity to satisfy the integral condition $\int_{-\infty}^{\infty} F^{y*}(X *)dX * = 1$ [Kljun et al., 2015]. The scaled footprint ensemble was used to fit the footprint parameterization for equation 6 using an unconstrained nonlinear optimisation technique based on the Nelder-Mead simplex direct search algorithm [Kljun et al., 2015]. The values of the fitting parameters were determined to be a=1.452, b= -1.991, c=1.462, d=0.136. For equation 8, the fitting function was chosen in conformity with Dearforff and Willis and the fitted data was a direct result from the simulations from LPDM- B [Kljun et al., 2015]. The values of the fitting parameters were found to be a_c=2.17, b_c=1.66, and c_c=20.0. Similarly, $\hat{\sigma}_y *$ is inserted into the non-dimensional standard deviation of the crosswind distance, given by:

$$\sigma *_y = p_{s1} \frac{\sigma_y}{z_m} \frac{u_*}{\sigma_v} \tag{9}$$

to derive the standard deviation of crosswind distance σ_y, which is dependent on the boundary layer conditions and the upwind distance. p_{s1} is a proportionality factor that depends on stability [Klijun et al., 2015] and is based on the LPDM-B results. Here, p_{s1} = min (1 ,$|z_m/L|^{-1}$ 10^{-5}+ p); where p =0.8 for $L \leq 0$ and p=0.55 for $L \geq 0$. The Gaussian function is well-suited for crosswind dispersion over complex surfaces and its characteristic for the entire stability range.

The non-dimensional form of the crosswind integrated footprint is:

$$F^{y*} = \overline{f^y} z_m (1 - \frac{z_m}{h})^{-1} (ln(\frac{z_m}{z_0}) - \psi_M) \tag{10}$$

$\hat{F}^{y*}$can then be inserted into equation 10 for F^{y*} and inverted to derive the crosswind-integrated footprint function $\overline{f^{y}}$. With all the parameters now available, the flux footprint can be evaluated using the following equation:

$$f(x,y) = \overline{f^{y}}(x)\ \frac{1}{\sqrt{2\pi\sigma_y}} exp(-\frac{y^2}{2\sigma^2{}_y}) \quad (11)$$

Here y is the crosswind distance from the centreline (i.e. the x axis) of the footprint.

The model has the advantage of being able to handle a wide range of boundary layer conditions, from convective to stable, for surfaces from very smooth to very rough, and for measurement heights from very close to the ground to high up in the boundary layer. Additionally, this model is applicable for daytime and nighttime measurements and for measurements from small and tall towers.

2.3.1: 1D Footprint

Hsieh et al., 2000 developed an approximate analytic expression, analogous to the Gash model, that accurately described the relationship between footprint, observation height, surface roughness, and atmospheric stability. The Gash model was a simple model for footprint calculation for neutral which was supersede by the Horst and Wiel model which is still used to the day. The drawback of the Horst and Wiel model is that even though it includes some consideration of how atmospheric stability affects fetch, this aspect is not clearly or directly articulated within the model. The reason this model is implemented over the Horst and Weil as in Conte and Contini (2019) because the Horst and Wiel model does not explicitly describe the relationship between footprint, atmospheric stability, observation height, and surface roughness, whereas the Hsieh et al (2000) analytical model more accurately describes the relationship of those parameters.

The Gash analytical model states the mathematical flux and footprint are related by:

$$F(x, z_m) = \int \int_{\infty}^{x} S\,(x) f(x, z_m) dx\, dy \qquad (12)$$

Where *F* is the scalar flux, *f* is the footprint, *S* (g m^{-2} s-^{1}) is the source strength, z_m is the measurement height, and the mean wind direction is along the horizontal coordinate is *x*. Gash's footprint model used the following solution for the advection diffusion equation in a neutral atmosphere with a uniform mean wind field U_u to derive

$$x = \frac{-(U_u z_m)}{k u_*} \frac{1}{ln\,(\frac{F}{S_o})} \qquad (13)$$

Where x is the fetch requirement (downwind distance) to achieve the desired normalized flux, F/S_0, u_* the friction velocity and *k* (=0.4) is von Karman constant. The uniform mean wind field U_u is defined as:

$$U_u(z_m) = \frac{u_*}{k}(ln\left(\frac{z_m}{z_0}\right) - 1 + \frac{z_0}{z_m}) \qquad (14)$$

Where z_0 represents the surface roughness. By rearranging (14), the relationship between flux and fetch is obtained as the following:

$$\frac{F(x,z_m)}{S_o} = exp\left(-\frac{U_u z_m}{k u_* x}\right) \qquad (15)$$

Using (12) and (15) Gash's analytical model to estimate footprint for a neutral atmospheric condition is:

$$f(x, z_m) = \frac{1}{S_0}\frac{dF(x,z_m)}{dx} = \frac{-(U_u z_m)}{k u_* x^2}\, exp\left(-\frac{U_u z_m}{k u_* x}\right) \qquad (16)$$

For a neutral atmospheric condition. The Gash model has many advantages as it is has the best model for describing the relationship between footprint, observation heigh and surface roughness. However, it is only applicable for neutral conditions as it does not include the effects of atmospheric stability. The fetch (x) is a function of F, z_m, z_0, and the atmospheric stability parameter (z_m/L), where L is the Obukhov length:

$$L = \frac{-u_*^3 T}{kg(w\theta)}, \quad (17)$$

k=0.4 is the Von Karman constant, g=9.8km/h. w' is the perturbation in the vertical direction and θ is the potential temperature. From (13) and (14), z_m and z_0 can be combined to form a new length scale z_u, defined as:

$$z_u = z_m(ln\left(\frac{z_m}{z_0}\right) - 1 + \frac{z_0}{z_m}) \quad (18)$$

There are three characteristic length scales: x, L, and z_u, for dimensional analysis with L being the normalizing variable:

$$\frac{x}{L} = f(\frac{z_u}{L}) \quad (19)$$

x/L varies with z_u/L for unstable, stable, and neutral atmospheric conditions and x/L can be expressed as:

$$\frac{x}{L} = \frac{-1}{(k^2 ln\left(\frac{F}{S_0}\right))} D\left(\frac{z_u}{L}\right)^P \quad (20),$$

where D and P are similarity constants. Hsieh et.,al (2000) plotted how x/L varies with z_u/L for each atmospheric condition and by applying regression analysis to the result, found the values of D and P.

Table 2: D and P are similarity constants from which the values represent the value for different atmospheric conditions.

Atmospheric Condition	D	P
Unstable	0.28	0.59
Near neutral and neutral	0.97	1
Stable	2.44	1.33

Finally, by rearranging (20), the flux can be estimated by:

$$\frac{F(x,z_m)}{S_0} = exp\,(\frac{-1}{k^2 x} D z_u^P |L|^{1-P}) \qquad (21)$$

And the footprint by:

$$f(x, z_m) = \frac{1}{k^2 x^2} D z_u^P |L|^{1-P} exp\,(\frac{-1}{k^2 x} D z_u^P |L|^{1-P}) \; (22)$$

This model improves upon the Horst and Wiel footprint model since it considers the stability of the atmosphere which is an important parameter for footprint since size and shape the footprint vary with height, windspeed, and stability [Oke et al., 2017].

2.4: Video Analysis

The video camera was a security camera which recorded footage of the road. However, since there is no software preloaded into the camera which would give it capabilities to count vehicles, a program is written using OpenCV, an open-source library in Python which can extract the pixel intensity value information from the video image[“OpenCV Tutorial: Opencv Using Python - Javatpoint].

Figure 10: Snapshot of the video footage captured by the camera and how the lanes are divided.

To count the number of vehicles in each lane, four ranges of pixels from the video footage were summed to give an average grayscale value for each lane on the road (Figure 10). The average grayscale value in each lane for each frame is determined. Figure 11a provides an example of how the program works, where the car passing in lane one causes grayscale value change in all the lanes. However, since Lane 1 has the longest duration for the grayscale deviation, it counts one vehicle in that lane (Figure 11b). There are limitations and errors which arise from this form of image processing. First, the video analysis program cannot distinguish vehicles in multiple lanes, as shown in Figure 12a where the vehicles in lane 3 overlap the vehicles in lane 4. Since the program takes into account the longest deviation in the grayscale value, it only counts the vehicle in lane 3. Additionally, if a larger vehicle passes on the road, since it has the longest grayscale reduction the program only counts one vehicle. Figure 12c shows bus blocking all four lanes, thus the program only counts one vehicle and does not count any movement behind it. This method is effective in order to draw relationships between the time of day and number of vehicles per hour, and the number of vehicles on an hourly basis, however the program was tested against vehicle counts determined manually to evaluate the counting accuracy. This is further discussed in section 3.1.

a) b)

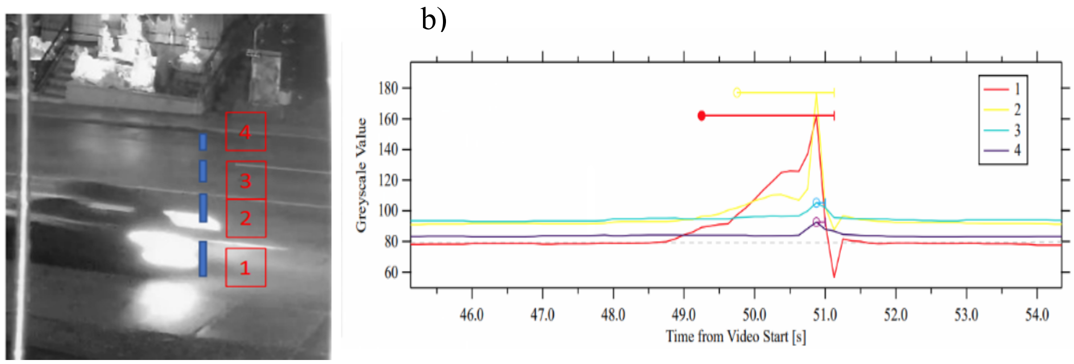

Figure 11: a) snapshot of the car passing in the lane 1. b) change observed in the greyscale value for each lane. It shows the longest change in the grayscale value occurs in lane 1.

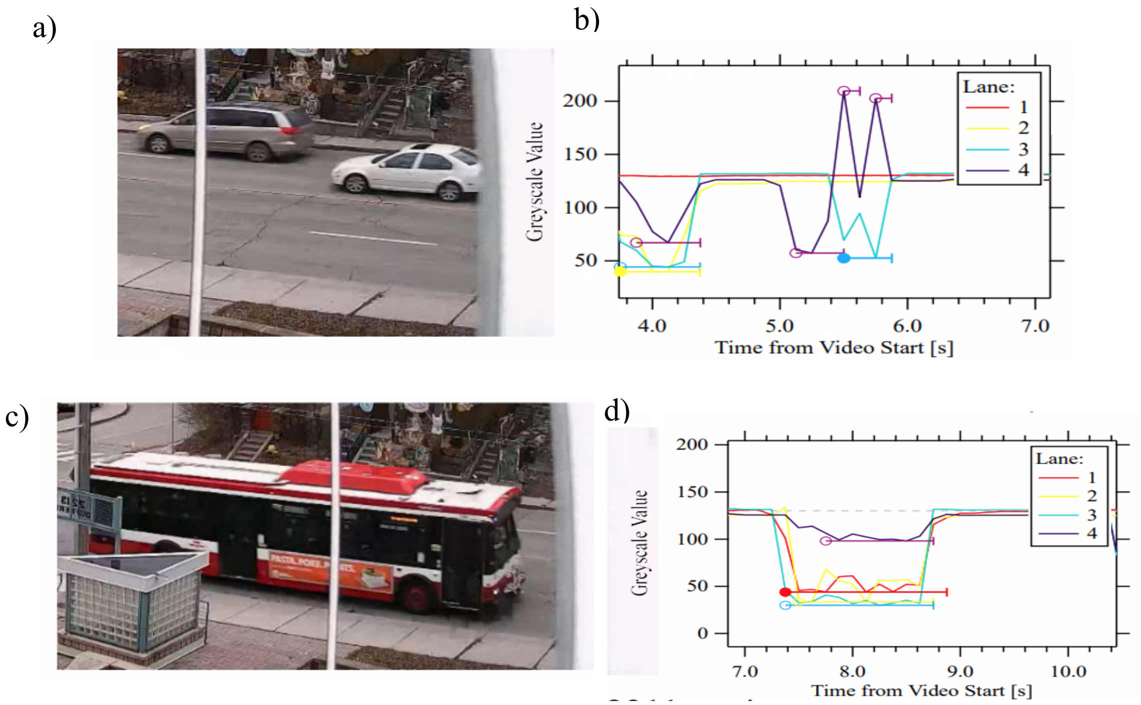

Figure 12: a) Snapshot of what the video footage observed with overlapping of vehicles. b) Change of the grayscale value where it does notice a vehicle in lane four however, since the vehicle in lane 3 overlaps the vehicle in lane 4 the duration of the vehicle in lane 4 is shortened so it only counts the vehicle in lane 3.c) Snapshot of what the video footage observes of the bus blocking all the lanes. d) Shows the grayscale values change in all lanes sense their bus is blocking them.

Chapter 3: Results & Discussion

3.1: Vehicle Count

Table 3 shows a comparison between manually counted vehicle data and the program output, with a focus on two periods: a period of minimal traffic at 1am, a morning rush hour period at 9am and an evening rush hour period for 7pm, for each month. The table indicates that the relative error for the selected dates is approximately 11.7%, representing an overestimation of vehicles. Note that January 6th to March 6th 1am and 7pm, as well as April 6th at 1am and May 6th at 1am, were all recorded in night mode (similar to Figure 10a), while all of the yellow highlighted periods were recorded in regular daylight (Similar to Figure 11a). During the night mode periods, there was an overcount of 49.4% by the program, while during the day, there was an undercount of 2.14% on average. The overestimation during the nighttime of vehicle counts is primarily caused by the brightness of headlights, which significantly alters the pixel intensity values in the video footage, complicating the accurate distinction of vehicles. Additionally, headlights illuminate the ground ahead of and beside the vehicle, causing the illuminated portion to move with the car. This movement can result in an inflated vehicle count, as the software may interpret the moving illuminated ground as an additional vehicle. For a visual representation of how ground illumination affects vehicle counting, refer to Figure 10 in Section 2.4. The undercount is likely due to the overlapping of vehicles in the lane. This means that vehicle counts made during the day are more accurate and reliable than those at night. It's important to note that during the study period, Toronto experienced several COVID-19 lockdown phases. These lockdowns significantly impacted vehicular traffic as many organizations implemented work-from-home policies, leading to a marked decrease in commuter traffic. According to a 2021 report by the City of Toronto, the lockdown measures enacted in January 2021 resulted in a reduction to 52% of typical vehicle traffic volumes during the morning peak hours (8 a.m. to 9 a.m.) and to 73% during the evening peak hours (5 p.m. to 6 p.m.), indicating a substantial decline in movement as residents adhered to public health directives ["City of Toronto Traffic Data Shows More People Staying Home to Fight COVID-19", 2021].

Table 3: This table provides an analysis of the relative error between the number of vehicles counted by the program and the number counted manually. The yellow highlighted time periods in the table represent instances when the video recording was done during daylight, while the gray highlighted periods represent instances when the video was recorded during night mode.

Date	**Time**	**Manual Count (vehicles/hour)**	**Program Output (vehicles/hour)**	**Relative error**
January 6	1:00am	178	384.6	116.07%
	9:00am	842	839.6	-0.29%
	7:00pm	1114	1394.5	25.17%
February 6	1:00am	214	368.1	72%
	9:00am	599	587.9	-1.85%
	7:00pm	1058	1376.9	30.14%
March 6	1:00 am	274	390	42.33%
	9:00am	671	650.5	-3.13%
	7:00pm	1109	1239.6	11.78%
April 6	1:00am	116	150.5	29.74%
	9:00am	1014	979.1	-3.44%
	7:00pm	932	903.3	-3.08%
May 6	1:00am	125	209.9	67.92%
	9:00am	906	898.9	-0.78%
	7:00pm	1035	1009.9	-2.43%

Figure 12 presents the average vehicle count during morning rush hour and evening rush hour for weekdays and weekends. The pink highlighted portions represent the missing data as the recording device had to be removed to download the data to prevent overwriting of files. It is missing data for the weekdays of February 9th to February 11th and March 19th to March 23rd. The average vehicle rate varies between 264 veh/h to 1390 veh/h. Table 3 shows the average vehicle count per hour for the morning rush hour, evening rush hour and off periods. It can be observed that the highest vehicle rate is during the weekday evening rush hour, with the weekday morning being a close second. Weekend mornings from 6 a.m. to 10 a.m. has the lowest volume of traffic compared to the evening, which has a significantly larger volume of traffic. Even during the off-peak period during the weekend, the average volume rate is larger than the traffic rate during the weekdays. This pattern can be intuitively expected and reflects traditional work schedule. Traffic grows later through the day during the weekend, whereas the weekdays have more distinct times as to when rush hour occurs. This correlates with activity during the weekends since people travel for recreational activities generally later in the morning into the evening on the weekend compered to weekdays. The data analysis for the vehicle count was processed using a Python code; however a check was done on the calculation to make sure whether the vehicle count was correct or not.

Expanding on the current video analysis technique, future research will include the use of computer vision and deep learning techniques to analyze the video data. Open-source technologies such as OpenCV, PyTorch, YOLO, and DeepSort will be used for object identification and tracking of vehicles to automatically determine vehicle class, vehicle speed and the presence of vehicle braking.

Table 4: Comparative Average Vehicle Counts per Hour During Various Dayparts. This table presents the average number of vehicles per hour during morning and evening rush hours, as well as off-peak times, for both weekdays and weekends.

Daypart	Weekdays (Vehicles/h)	Weekend (Vehicles/h)
Morning Rush Hour (6 a.m. to 10 a.m.)	856	366
Evening Rush Hour (3 p.m. to 7 p.m.)	1202	1097
Off-Peak (10 a.m. to 2 p.m. and 8 p.m. to 5 a.m.)	627	633

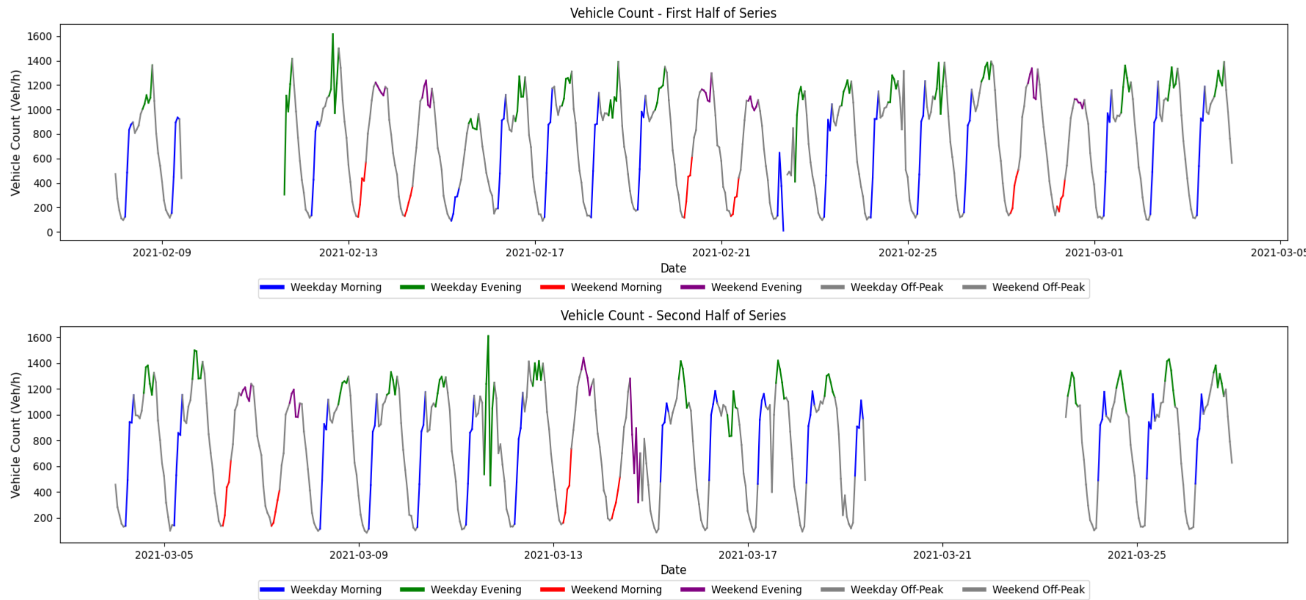

Figure 13: This line graph depicts the comparison of average vehicle counts during rush hours on weekdays versus weekends over a specific period. Distinct colors signify specific times and days: blue for weekday mornings, orange for weekday evenings, green for weekend mornings, red for weekend evenings, and grey for off-peak travel periods. Vertical pink bars highlight the intervals where data is absent due to the necessity of removing the recording device for data retrieval. The graph demonstrates the variability in traffic volume, typically showcasing higher vehicle counts during weekday rush hours as opposed to weekends. Notably, the data points reveal considerable fluctuation, with the highest vehicle counts occurring on weekday evenings and the lowest on weekend mornings.

3.2: Footprint Analysis

The spatial distribution findings from the flux footprint analysis provide insights into pinpointing the origins of particle flux. Figure 14 shows the relationship between the footprint flux and the road. The spatial footprint represents an average derived from 30-minute intervals over the entire study period. The individual footprints were calculated when the wind- direction was from 180-270° The footprint increases with distance initially, peaking just past 50 m, and then decreases. With the peak being just within the length of the road, it implies that the influence on the measured flux is greatest from the road and beyond the road the influence begins to dimmish. The average footprint flux over the entire study periods is 0.0089 m^{-1}. Conte and Contini (2019) had very similar results, with the footprint flux within their study being 0.005

m^{-1}. This suggests that the measured flux is more sensitive to the particulate matter originating from the road and that the influence of emissions is significantly lower upwind from the road when averaged over the entire study period. Together, these plots suggest a spatial relationship in which emissions from the road contribute significantly to the measured flux when the wind is perpendicular to the road.

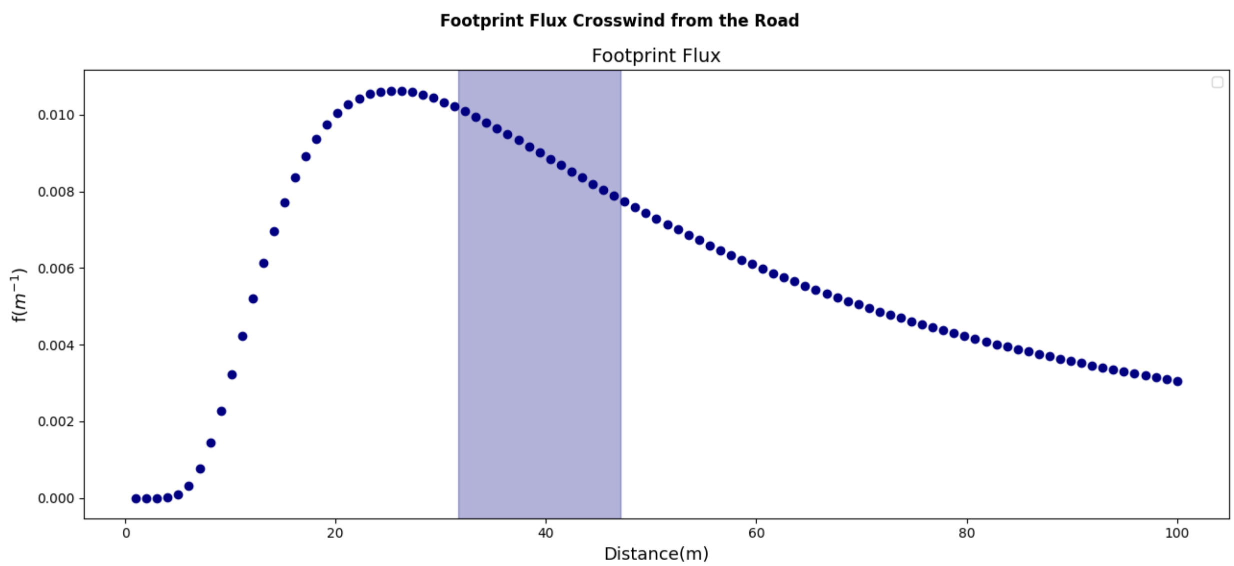

Figure 14: Analysis of the footprint flux influenced by crosswind from the road. The footprint flux (f [m^{-2}]) against distance, showing an initial increase and subsequent decrease, with the peak located within the blue shaded area representing the road's influence upwind.

The 2D footprint flux data for the analysis were obtained directly from Kljun, who have made their model publicly available. Figure 14 illustrates the 2D footprint or spatial distribution of fluxes in the *x* and *y* directions. The footprint was calculated using 30-minute averages throughout the study period for the selected wind direction of 180-270°. The model accounts for both stable and unstable environments; however, it does not accommodate stability parameters below -15.5. Consequently, only values greater than -15.5 were used. The average wind direction was 215°, and the average stability parameter indicated a weakly stable environment at 0.12.

Additionally, the model requires the friction velocity to exceed 0.1 m/s to avoid calm conditions. The average friction velocity in this study was 0.533 m/s, but instances below 0.1 m/s were excluded as the model stipulates a minimum of 0.1 m/s.

The contour lines on the plot represent the contributing source areas for varying percentages of the total flux, 10, 20, 30, 40, 50, 60, 70, and 80%, estimated by the tower. The 2D footprint is markedly smaller than the 1D footprint, 0.0006 m^{-2} compared to 0.0089 m^{-1}, respectively, and shows the peak of the contribution at 11 m upwind from the station. When comparing the 1D footprint to the 2D footprint as a function of x alone, the footprint is 0.0044 m^{-1}, indicating that the 2D footprint is compares well with the 1D footprint, although it remains smaller than the value from the 1D. This may be attributed to the 2D model's limitations in this environment. Since the FFP is based on LPDM-B simulations, the application limits of LPDM-B also apply to FFP. LPDM-B does not account for dispersion within the roughness sublayer near the ground or the entrainment layer at the top of the convective boundary layer. Therefore, it was recommended to limit FFP simulations to measurement heights above the roughness sublayer and below the entrainment layer. However, the experimental site setup was within the roughness sublayer, making it less suitable to apply this model to our study. Moreover, footprint parameterization was evaluated for the range specified in Table 4, and it was noted that application beyond this range should be approached with caution. Comparisons with average results from this study indicate that the values fall outside this specified range, thus their applicability cannot be guaranteed.

Even though the 2D footprint was not helpful to in concluding whether the entire study period indicted that fluxes were indeed from the road it was helpful in identifying that under a stable environment vehicle traffic contributes to the source of the fluxes.

Table 5: Parameters evaluated for the 2D footprint analysis by Kljun et al., 2015.

Scenario	Frictional Velocity (u^* [ms^{-1}])	Convective Velocity (w^* [ms^{-1}])	Obukov Length (L [m])	Boundary Layer (h [m])
Convective	0.2	1.4	-15	2000
Convective	0.2	1.0	-30	1500
Convective	0.3	0.5	-650	1200
Neutral	0.5	0.0	∞	1000
Stable	0.4	--	1000	800
Stable	0.4	--	560	500
Stable	0.3	--	130	250
Stable	0.3	--	84	200

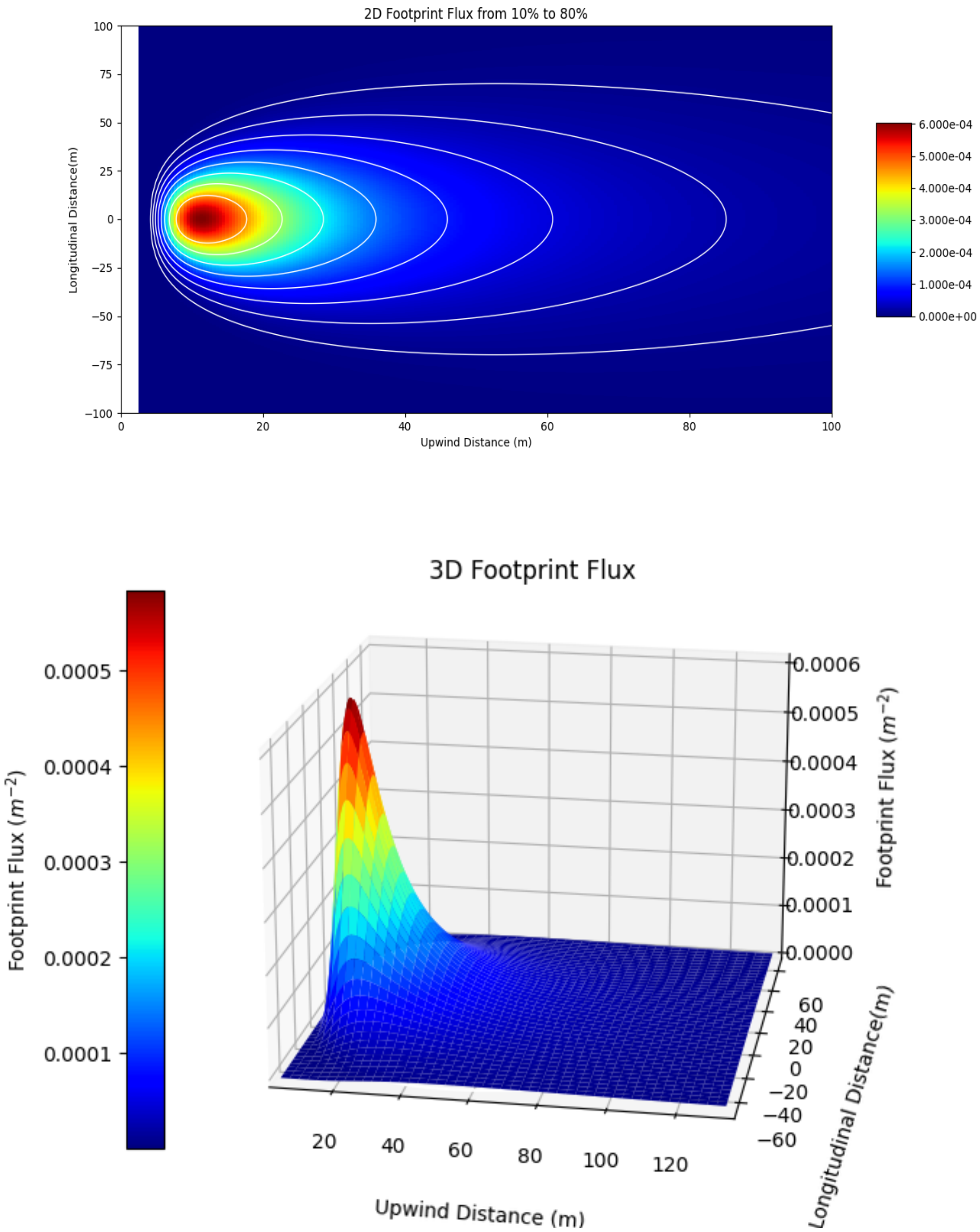

Figure 15: Average footprint flux calculated for the entire study period, showing contributions from 10% to 80%. (a) 2D footprint flux, (b) The 2D footprint flux represented on a 3D plane to better illustrate the magnitude.

3.3: Characteristic of particle size distribution

Understanding the distribution of concentrations helps to break down the distribution of particles within categories further to better understand the dominance of particle sizes throughout the data collection. This is particularly important when discussing the lifetime of airborne particles, since ultrafine particles (< 100 nm) have a longer lifetime in the atmosphere compared to larger particles. This longevity could account for a higher concentration, as well as indicate the source of the concentration as being from a different location. Examining individual bin concentrations allows us to gather information about the dynamics of ultrafine particles and fine particles separately and to understand the dominating particle sizes. These size ranges are important for their effects on human health, especially regarding the small particles related to urban emissions, mainly due to road traffic [Zhang and Batterman, 2013; Pérez et al., 2010].

Organizing concentration data according to peak traffic times- the morning and evening rush hours - reveals that ultrafine particles (< 100 nm) overwhelmingly influence the number concentration distribution, showing contributions of 10^2 particles/cm^3. In contrast, particles exceeding 500 nm do not surpass an average of 10 particles/cm^3 throughout the study. There is a higher concentration of particles in the morning, which could stem from the nocturnal buildup of pollution within the stratified boundary layer. This layer's subsequent dilution with fresher air leads to increased vertical particle movement [Conte et al., 2017], culminating in a pronounced morning concentration despite higher vehicle counts in the evening. Table 1 (section 3.1) outlines the average vehicle count values.

The analysis over a five-week period from February 9 to March 19 shows a steep decline in particle concentration from 60 nm to 100 nm, during both rush hour periods (Figure 16a-d). However, for the two weeks following (March 19 – March 23), there is a less severe drop in the average ultrafine particle concentration. This interval records an increase in the particle concentration by 15x for particles sizes over 100 nm. The observed increase in particles larger than 100 nm could be due to a rise in particulate matter carried from upwind, which is detected at the site. Particles ranging from 30 nm to 1000 nm in size fall within the accumulation mode. They have a longer atmospheric lifetime, averaging 7-30 days, making it highly probable for particles originating from upwind sources to be present.

Particle size distribution is separated into three mode: nucleation mode, accumulation mode, and coarse mode. Nucleation mode corresponds to particles that have been formed from gaseous molecules and later grow via condensation and coagulation, generally occurs with sizes < 50 nm [Kwon et al., 2020] (For more of an in-depth explanation refer to section 1.1). Particle dynamics within the 30 nm to 1000 nm range are governed by the accumulation mode, a critical phase wherein particles can augment via condensation and coagulation, remaining airborne for extended durations [Kwon et al., 2020]. Within this study, the range of 100 nm to 1000 nm is categorized under accumulation mode, where particles evolve from fine particle emissions and enlarge through condensation and coagulation events [Kwon et al., 2020]. The inefficiency of removal mechanisms in this mode leads to the accumulation of particles, which can persist for 7-30 days until eventually removed due to rainfall or precipitation events [Kwon et al., 2020]. Therefore, understanding particle concentrations from vehicular sources as opposed to background levels is essential for assessing the true origin of emissions.

When comparing the concentration from the road vs background February 9 to February 18, the morning rush hour showed there was a high concentration of particles along all size ranges coming from a background source rather than from the road. The names “road” and “background” do not refer to the concentration coming from the road itself; rather, they refer to the wind direction, which is 180°-270° for road and 90°-170° for background. In fact, the particles may originate from upwind external sources. In the evening, however, there is a high concentration ranging from 55 nm to 61 nm coming from the road; beyond that point most of the concentration is coming from an external source. From February 18 to March 5th, the morning concentrations linked to background winds consistently exceeded those associated with wind directions from the road, with a notable increase for particle sizes between 73 nm to 98 nm from the road during the period from February 18th to February 26th. The following week showed a slight rise in road-related particles ranging from 93 nm to 172 nm but beyond that point background concentration supersede. Evening comparisons for the same intervals presented a contrasting pattern, with background concentrations dominating except for the week of February 26th to March 5th, which showed an increased presence of road-sourced particles up to 150 nm.

For the period between March 19th and March 23rd, evening concentrations were predominantly higher from road emissions across all measured sizes. This contrasted with morning data, where particles from 60 nm to 80 nm were more abundant from background sources, but larger particles demonstrated a significant increase from road sources. Conte et al. (2019) reported analogous findings, noting that particles smaller than 250 nm dominated the number concentration distribution (10^4 particles/cm^3) compared to their larger counterparts.

On the other hand, for the periods of March 19th to March 23th and March 23th to March 26th particles > 500 nm had a higher concentration from the road for both the morning and evening compared to the background. However, for the weeks prior, February 9th to March 19th, there is a greater concentration coming from background sources compared to the road.

Hence, calculating turbulent flux and the footprint is imperative. Turbulent flux assessments help determine whether particles are being emitted from or deposited onto a particular site, while footprint analysis ascertains the source area of the flux. Such analyses are helpful in confirming if collected concentrations are indeed influenced by vehicular traffic or external sources.

a)

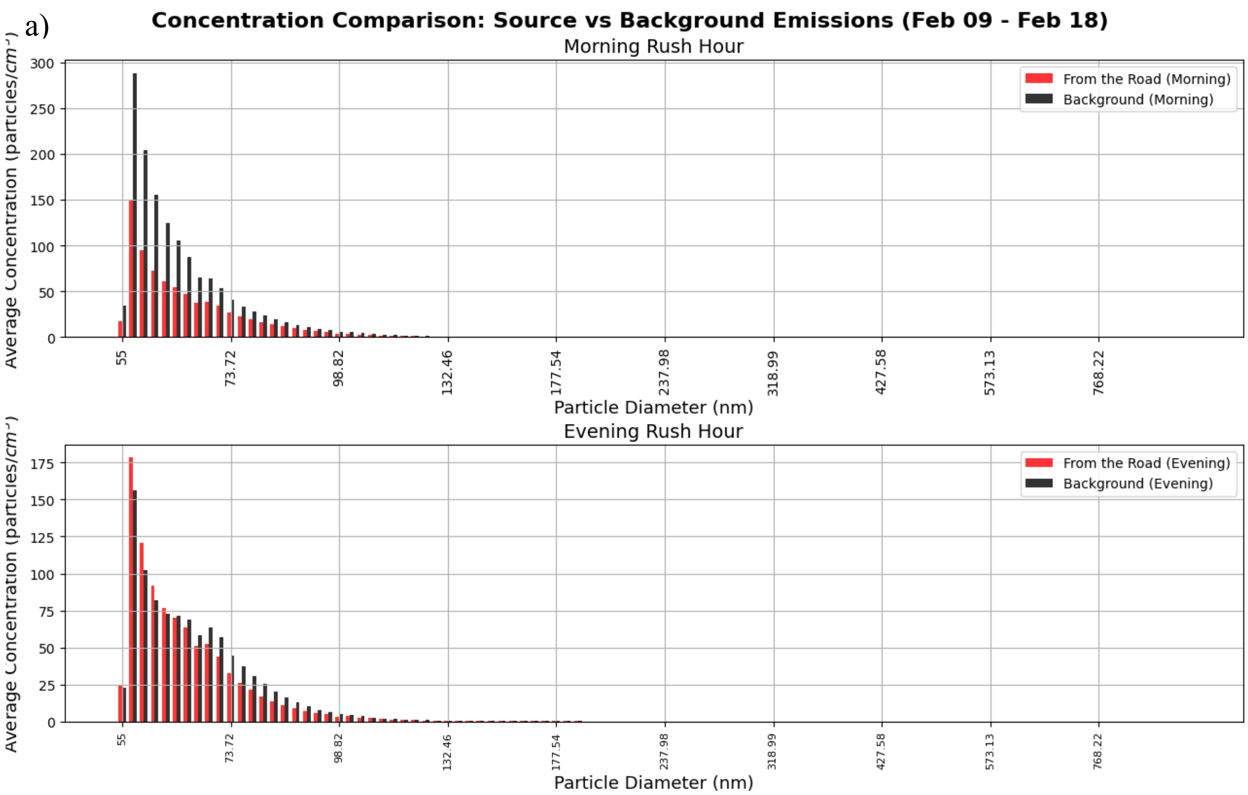

b)

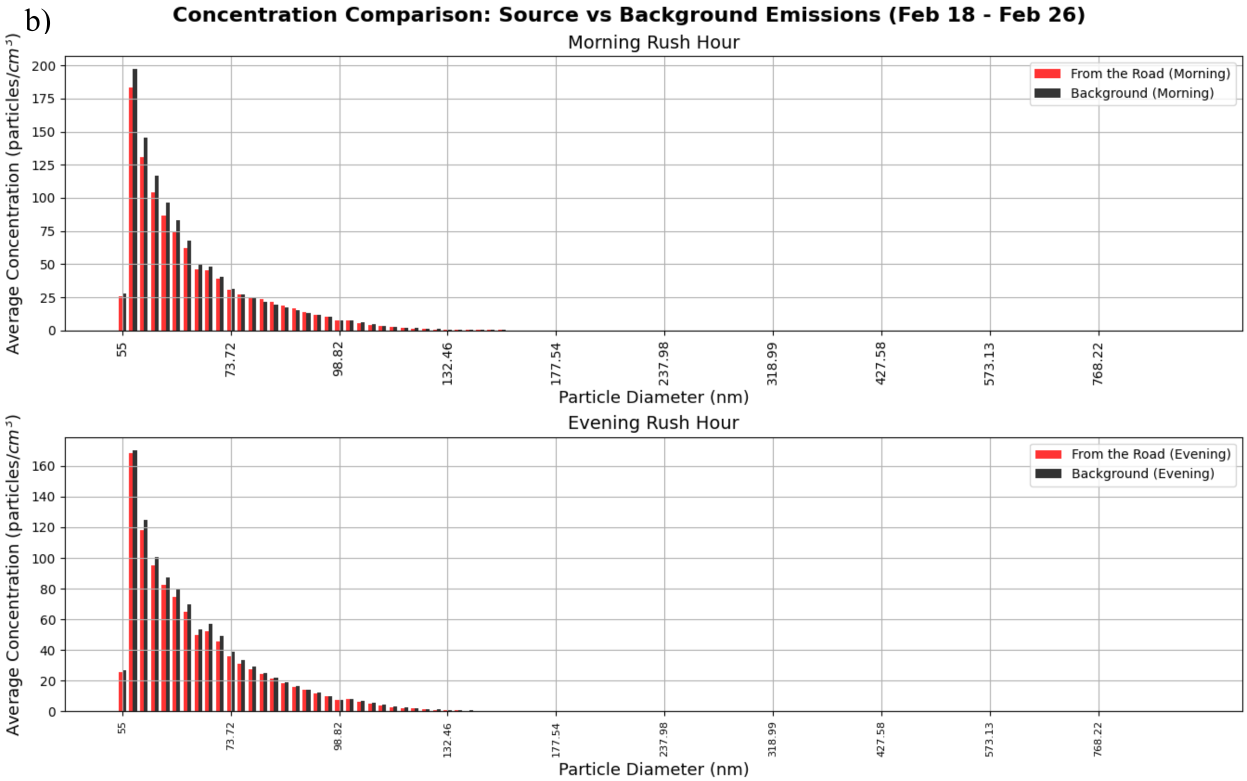
Concentration Comparison: Source vs Background Emissions (Feb 18 - Feb 26)
Morning Rush Hour
From the Road (Morning)
Background (Morning)
Average Concentration (particles/cm³)
Particle Diameter (nm)
55
73.72
98.82
132.46
177.54
237.98
318.99
427.58
573.13
768.22
Evening Rush Hour
From the Road (Evening)
Background (Evening)
Average Concentration (particles/cm³)
Particle Diameter (nm)

c)

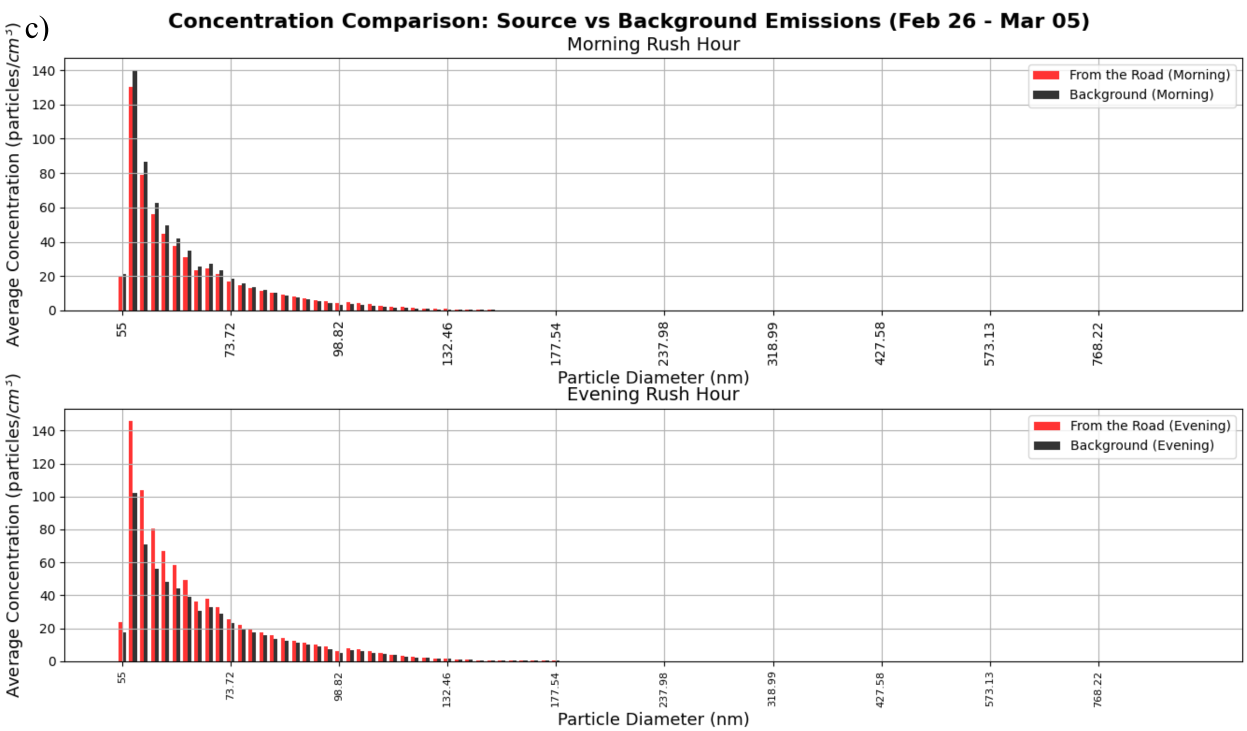
Concentration Comparison: Source vs Background Emissions (Feb 26 - Mar 05)
Morning Rush Hour
From the Road (Morning)
Background (Morning)
Average Concentration (particles/cm³)
Particle Diameter (nm)
55
73.72
98.82
132.46
177.54
237.98
318.99
427.58
573.13
768.22
Evening Rush Hour
From the Road (Evening)
Background (Evening)
Average Concentration (particles/cm³)
Particle Diameter (nm)

d)

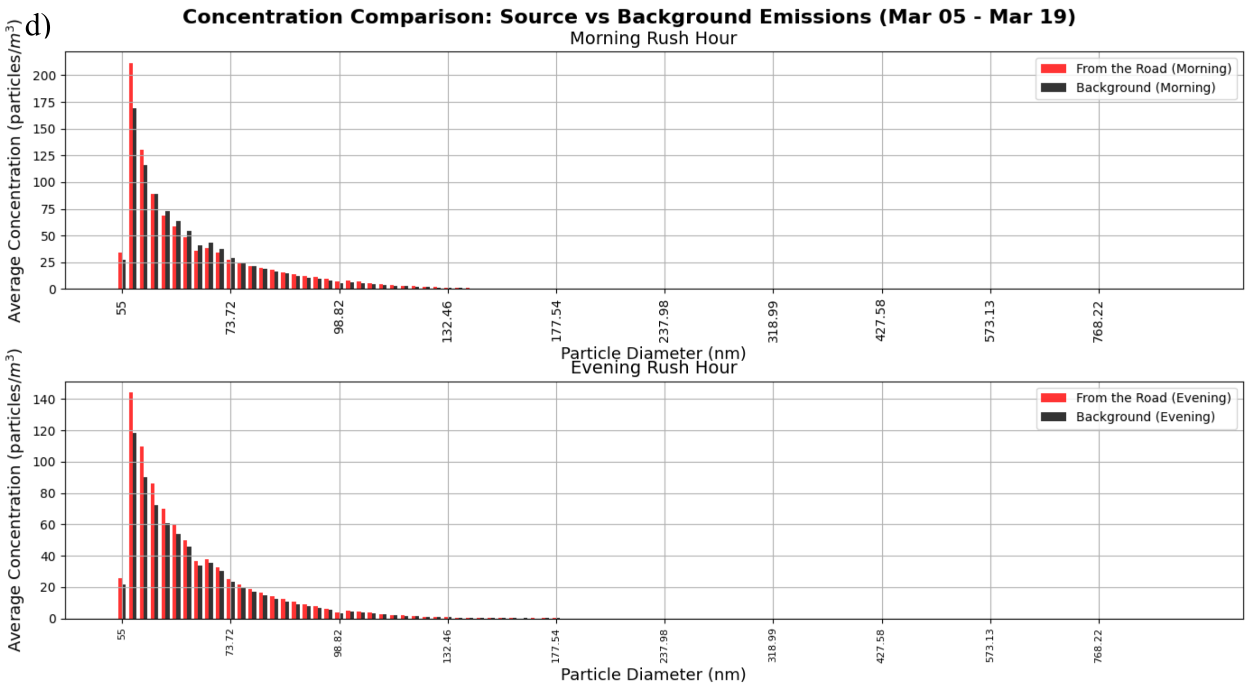
Concentration Comparison: Source vs Background Emissions (Mar 05 - Mar 19)
Morning Rush Hour
From the Road (Morning)
Background (Morning)
Average Concentration (particles/m^3)
0
25
50
75
100
125
150
175
200
55
73.72
98.82
132.46
177.54
237.98
318.99
427.58
573.13
768.22
Particle Diameter (nm)
Evening Rush Hour
From the Road (Evening)
Background (Evening)
Average Concentration (particles/m^3)
0
20
40
60
80
100
120
140
55
73.72
98.82
132.46
177.54
237.98
318.99
427.58
573.13
768.22
Particle Diameter (nm)

e)

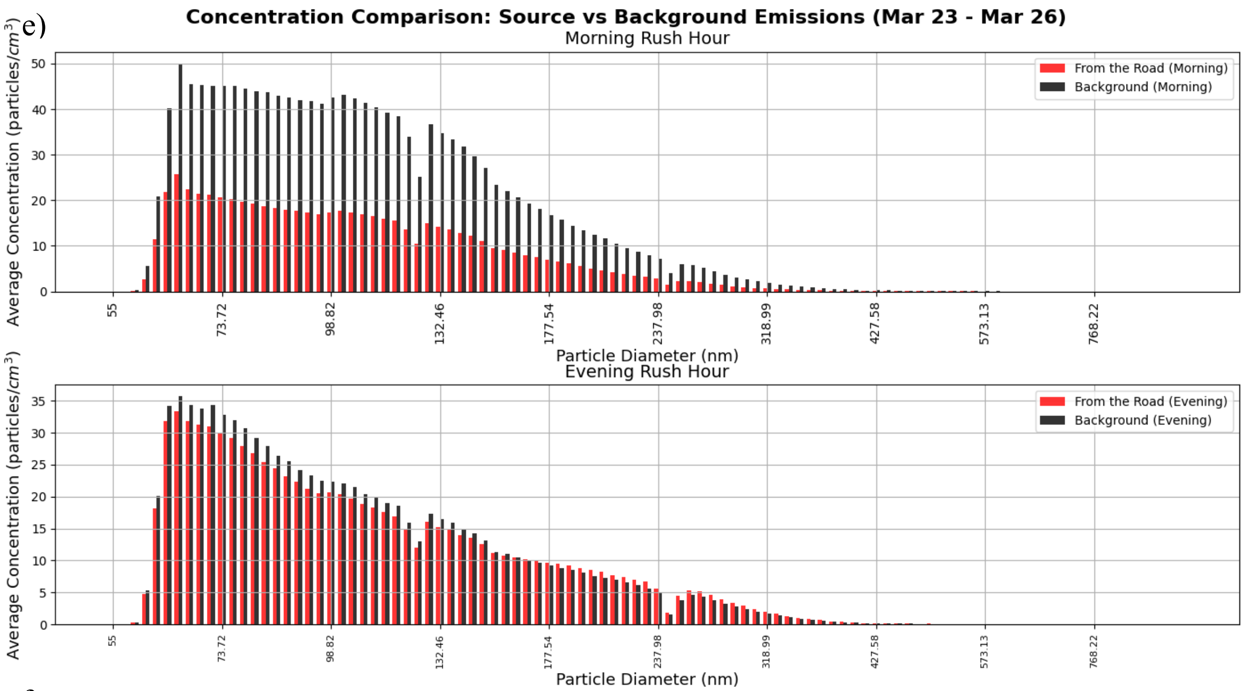

f)

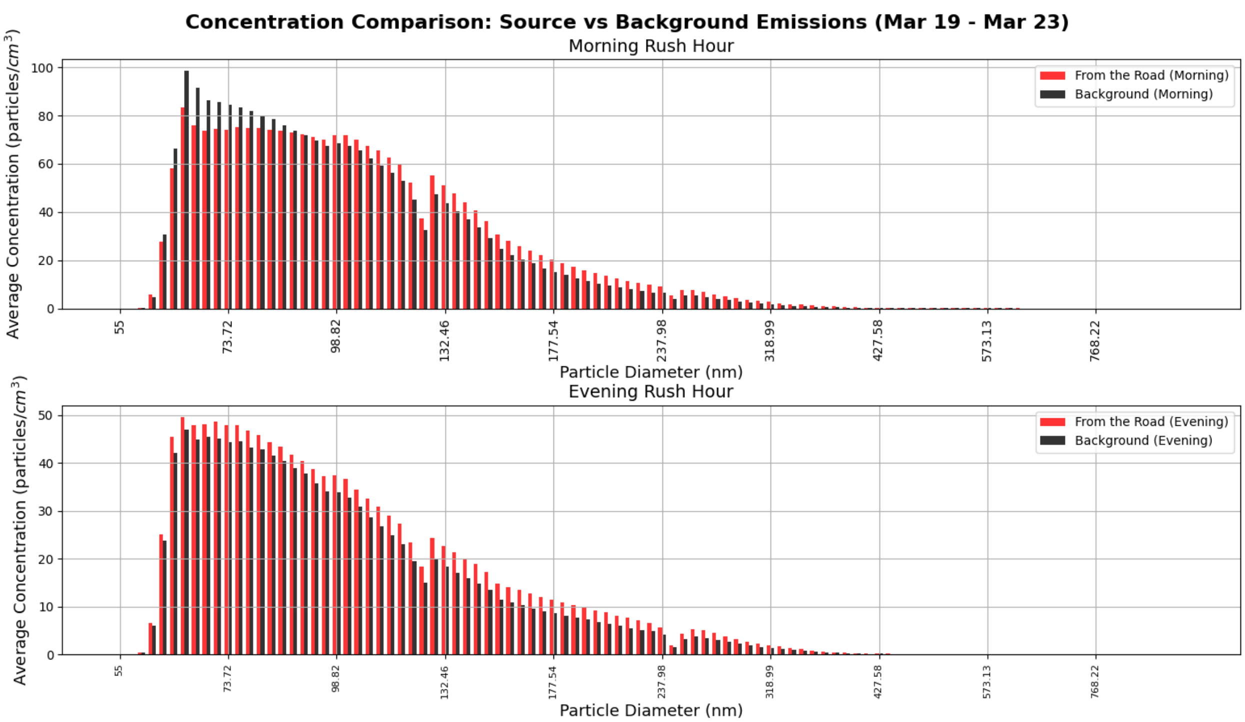

Figure 16a-f: Particulate Matter Size Distribution During Morning and Evening Rush Hours Over Two-Week Periods. The histograms compare the average concentration of particles, differentiated by diameter size, from road emissions (red) versus background levels (black) during the morning (top) and evening (bottom) rush hours. This not presented as an average of the entire study period because external sources over a weekly or bi-weekly period can significantly skew the results.

3.4: Calculation for size-segregated particles from road and background

The particle number fluxes were evaluated using turbulent flux measurements with the eddy-covariance method. To better understand the fluxes and emissions, a turbulent flux analysis is conducted for fluxes which originated from the road and those that originated from an outside source. Comparing the concentration measurements from the road with those from background sources, alongside the turbulent flux data, provides a clearer resolution as to whether the observed concentrations originate from vehicular traffic or are attributable to background sources. The wind direction from 180° to 270° would carry emissions emitted from the road to the station. To evaluate background sources, on the other hand, wind direction from 90°-170° was chosen, especially because 90° to 170° with respect to the station covers an area with tall dense trees and no source of particulate matter. From the results of the turbulent flux for both sets of particle sizes, there was a mixture of positive and negative fluxes. When comparing the average turbulent flux measurements over the studied period with the wind direction from 180°-270° smaller particle sizes (between 60 nm to 499 nm) resulted in an average flux of -9.84×10^5 particles/m^2s and the particles > 500 nm had a flux of 74.98 particles/m^2s. Negative fluxes indicate deposition, whereas positive fluxes indicate emission [Conte and Contini., 2019]. Negative fluxes for relatively large particles were also observed in other urban areas [Deventer et al., 2013; Conte et al., 2017; Conte and Contini., 2019] and they could be due to different dynamics of coarse particles and/or influence from traffic sources located at a larger distance ftom the measurement sites [Conte and Contini., 2019]. In this study, larger particles exhibited a net positive flux, indicating that there was a net emission of larger particles. However, measured fluxes represent the net effect of vertical movement due to turbulence, which includes both emissions into the air and depositions back to the surface happening concurrently [Conte and Contini., 2019]. This suggests that the actual amount of pollution from traffic could be higher than what is detected by these measurements since the measurement can't differentiate between emissions and deposition happening at the same time [Conte and Contini., 2019]. Therefore, there might be an underestimation of the real amount of pollution coming from traffic, leading to less accurate calculations of its impact. In other studies, to investigate deposition process (negative fluxes) or net emission processes (positive fluxes) the individual fluxes were separated accordingly [Pellenn et al., 2017; Deventer et al., 2015; Martensson et al., 2006; Held and Klemm, 2006; Lamaud et al., 1994, Conte and Contini., 2019], while other authors [Nemitz et al., 2002] preferred to keep all fluxes without distinction. Nonetheless, a deposition cannot be used to investigate vehicle emissions.

With the smaller particles resulting in an average flux which is negative, this is representative of a net deposition rather than emission over the complete analysis period. Negative fluxes for ultrafine particles were observed during Donateo et al. (2021) and Straaten et al. (2022), which investigated the impacts of the Covid-19 lockdown on vehicular emissions. It was concluded that there was an increase in the deposition of ultrafine particles as external sources persisted and the reduction in vehicular traffic transformed roads from sources into sinks. Since the overall flux rate is significantly larger for smaller particles than larger sized particles, this implies there was a greater number of smaller particles in the atmosphere compared to larger particles. When comparing this to the net background flux, -1.66×10^{5} particle/m^{3}, which is also negative, this implies smaller particles from background sources are also depositing. However, on average, fluxes from the road are greater than the background. It is worth noting that fluxes arising from what is denoted as the background can have vegetation interference. Deshmukh et al (2018) conducted a study which investigated the effects roadside vegetation played on near road air quality and reported that when their roadside vegetation consisting of tall dense vegetation with low porosity saw an average downwind pollutants reduction of approximately 30% with a 50% reduction in ultrafine particles. Trees were characterised as low porosity [Deshmukh et al., 2018], indicating that the background emission concentration may be significantly higher than what is collected. Furthermore, the deposition may be due to the construction along Eglinton Ave West, Toronto, ON, Canada during the time of the study. Located approximately 500 m NW of the study site combined with road slopping downward along Dufferin street this could be one of the sources of deposition for smaller particles. A study conducted by Alshetty and Nagendra, 2021, about road dust resuspension and distribution during construction activity found that larger particles (PM_{10}) at a range of 400-500m had an average concentration of 100-150µg/m^3, concluding that heavy duty trucks largely influenced the resuspension of road dust in surrounding areas.

The average turbulent flux for particles greater than 500 nm from the road is positive, indicating net emissions, whereas it is negative for background sources, indicating deposition. Conte et al., 2017 also suggested that the increase in negative fluxes for larger particles could represent an increase in deposition velocity, suggesting a possible influence from sources not related to vehicular traffic. This correlates with fluxes from the background, as the direction of 90°-170° represents an area of minor roads with very limited traffic. Additionally, the deposition in the background may be due to the construction along Eglinton Ave West, Toronto, ON, Canada during the time of the study. When individually analyzing the bi-weekly averages for the larger particles the particles from the background show a positive flux the period between March 5th to March 19th. This timeframe has a positive flux for both, on road and background sources whereas every other week there seems to be more deposition than emissions from the road, indicating some error in the collection for that particular bi-weekly period or there was a lower amount of emission.

a) b)

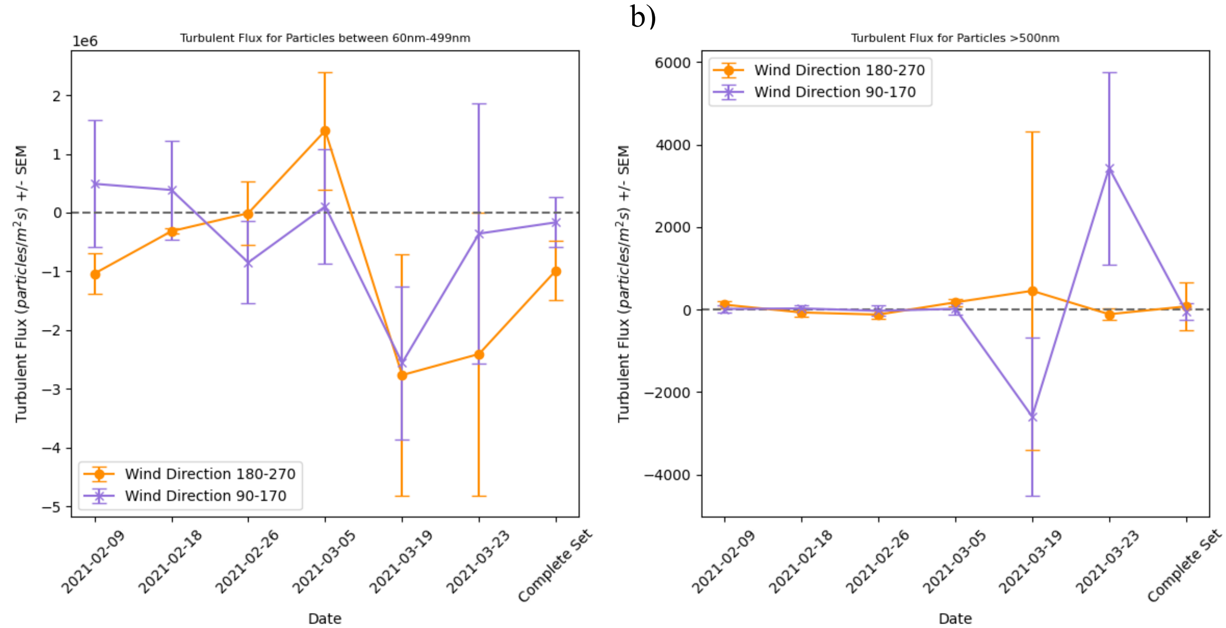

Figure 17: Temporal variation in turbulent flux for particulate matter of different sizes. a) displays turbulent fluxes for particles between 60nm-499nm, while b) shows those for particles >500nm.In both panels, the fluxes are categorized by wind direction: orange represents wind from 180-270 degrees and purple represents wind from 90-170 degrees. Error bars indicate the standard error of the mean (SEM) for each data point. The "Complete Set" refers to aggregated data over the entire measurement period.

Table 6: Provides the quantitative values of the average flux and associated standard error for the entirety of the study period.

Wind Direction	60 nm < Particle Size < 500nm *Units: particles/m^2s*	Particle > 500 nm *Units: particles/m^2s*
Road (180°-270°)	-9.84×10^5 SE: 4.98×10^5	74.98 SE: 589.33
Background (90°-170°)	-1.66×10^5 SE: 4.25×10^5	-43.28 SE: 201.29

The standard error of the mean gives an indication of how accurate the average turbulent fluxes are. For both smaller and larger particle sizes there is large variability in the data, as shown in Table 5. For the larger particles the standard error is significantly larger than the magnitude of the turbulent flux which suggests that there is large variability in the measurement.

Figure 18 shows the average turbulent flux values from the road vs the background, with the bars to representing the confidence interval of the average (95% probability). For the smaller particles, the width of the confidence interval is quite large, indicating there is a significant amount of variability in the measurement compared to the larger particles. With the larger particle sizes, the confidence interval is large and centered near zero, indicating that there may not be a significant transport of particles happening at all. With the confidence interval spanning both negative and positive values (-1.08×10^4 particles/m^2s, 1.23×10^4 particles/m^2s), it implies the data is not indicating one consistent direction of flux. Similarly, for the background source of smaller particle emissions, there is no strong indication of either emission or deposition. From this information, the conclusion that can be drawn is that the transport of larger particle sizes is likely negligible or inconsistent. It is possible that 1 Hz is too slow to capture the vertical transport with eddy covariance, even though Conte and Contini (2019) used 1 Hz, a higher frequency, such as 10 Hz (implemented by Straaten et al., 2022) would have been more accurate for this location. The confidence interval centered near zero suggests that there is no significant evidence of a unidirectional flux, either emissions or deposition, of these smaller particles. Consequently, for larger particle emissions that might be considered background sources, the data does not provide a clear indication of their behavior. There isn't a significant signal to suggest that these particles are being emitted into the environment or being deposited from it in any substantial manner. This could imply that their presence in the system is relatively stable or that their movements are random and not driven by the processes or influences being studied.

For the smaller particles, the width of the confidence interval is quite large indicating there is a significantly higher amount of variability in the measurement compared to the larger particles. This could be due to errors in measurement or a small sample size, considering the data are filtered to only use measurements from when the wind direction is between the specific range. However, since the confidence interval does not cross zero (-1.96×10^6 particles/m^{2}s, -6.41×10^4 particles/m^{2}s], it suggests that the net deposition is not due to random chance or variability. With the background emissions, there is a high variability. However, with the range of the confidence interval being positive and negative (-1.00×10^6 particles/m^{2}s, 6.69×10^5 particles/m^{2}s), crossing the zero boundary, it cannot be concluded that there is a net emission or deposition for this data set. With the average flux measurement for the larger particles being -1.66×10^5 particles/m^{2}s, it lies in the lower half of the confidence interval, suggesting that there may be a true net flux. However, due to the confidence interval crossing zero, it is not definitive.

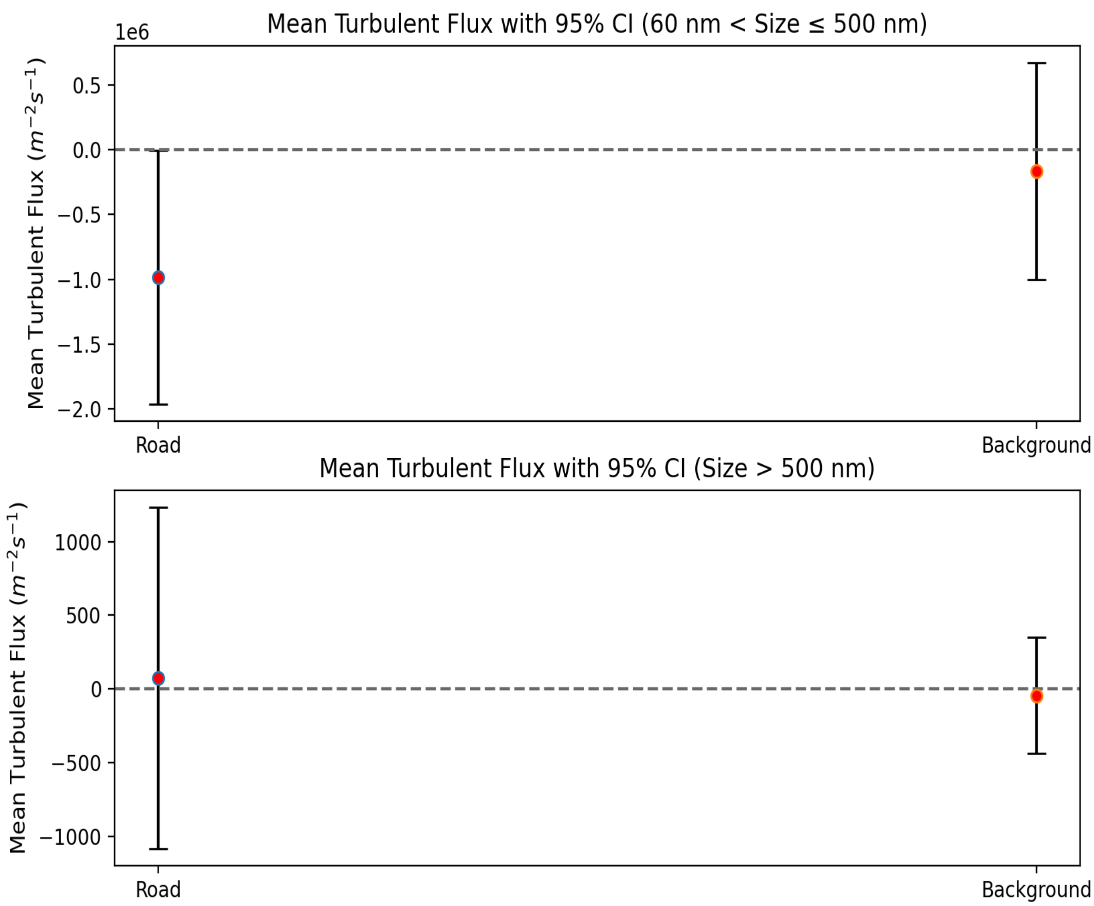

Figure 18: Depicts the net turbulent flux of particulate matter across different size ranges from road and background sources, with the 95% confidence interval of the mean underscoring the data's reliability.

3.5: Comparative analysis of turbulent flux of weekday vs weekend

During weekdays, the volume of traffic notably surpasses weekend levels, primarily due to the increased number of commuters traveling for employment and routine activities. Conversely, weekend traffic is predominantly characterized by leisure-oriented travel. This pattern is intuitively expected and reflects human activities in an urban area. The weekday emission flux for larger particles is 694.83 particles/m^2s. On the other hand, for smaller particles the emission flux is, negative, -9.60×10^5 particles/m^2s (Figure 17). This suggests that deposition was limited for larger sized particles whereas it was significant for smaller particles. The increased deposition flux suggests the of the source of the particles is not related to vehicle emission [Conte et al., 2017]. Similar results were found in Conte et al. (2017) and Deventer et al. (2013). Similarly, during the weekend, larger and smaller particles both had negative fluxes, 1.28×10^3 particles/m^2s and -1.10×10^6 particles/m^2s, respectively. Similar results were reported in Conte et al., 2017 where the deposition flux increased by 5% for smaller particles and 10% for larger particles during the weekend. The deposition rate for smaller particles increased by 14.58% for the weekend compared to the weekday deposition rate. The rise in particle deposition rates over weekends compared to weekdays could be linked to decreased traffic, leading to greater deposition from non-vehicular sources. This indicates that higher emissions from vehicles usually correspond to an upward trend in net flux.

The only net emission calculated for particles greater than 500 nm occurs during weekdays. Calculating the emission factor (EF) allows for quantification of the traffic-related particle strength. The emission rate for larger particles during weekdays is 3.05×10^9 #/ Veh km. The study by Conte and Contini (2019) calculated the emission factor (EF) and found an average EF of 2.2×10^{14} #/ Veh km, based on data collected in 2015. A similar campaign conducted in

2010 reported an EF of 5.0×10^{14} #/ Veh km. In the study by Conte and Contini (2019), the emission factor (EF) for particles between 500 nm and 1000 nm averaged in the order of 10^{14}. The lower EF observed in this study can be attributed to the emission rate being unable to overcome the downward flux from deposition, resulting in lower values. Traffic rates in the Conte and Contini study ranged from 380 to 1890 vehicles per hour, whereas in this study, the range was between 600 and 1200 vehicles per hour.

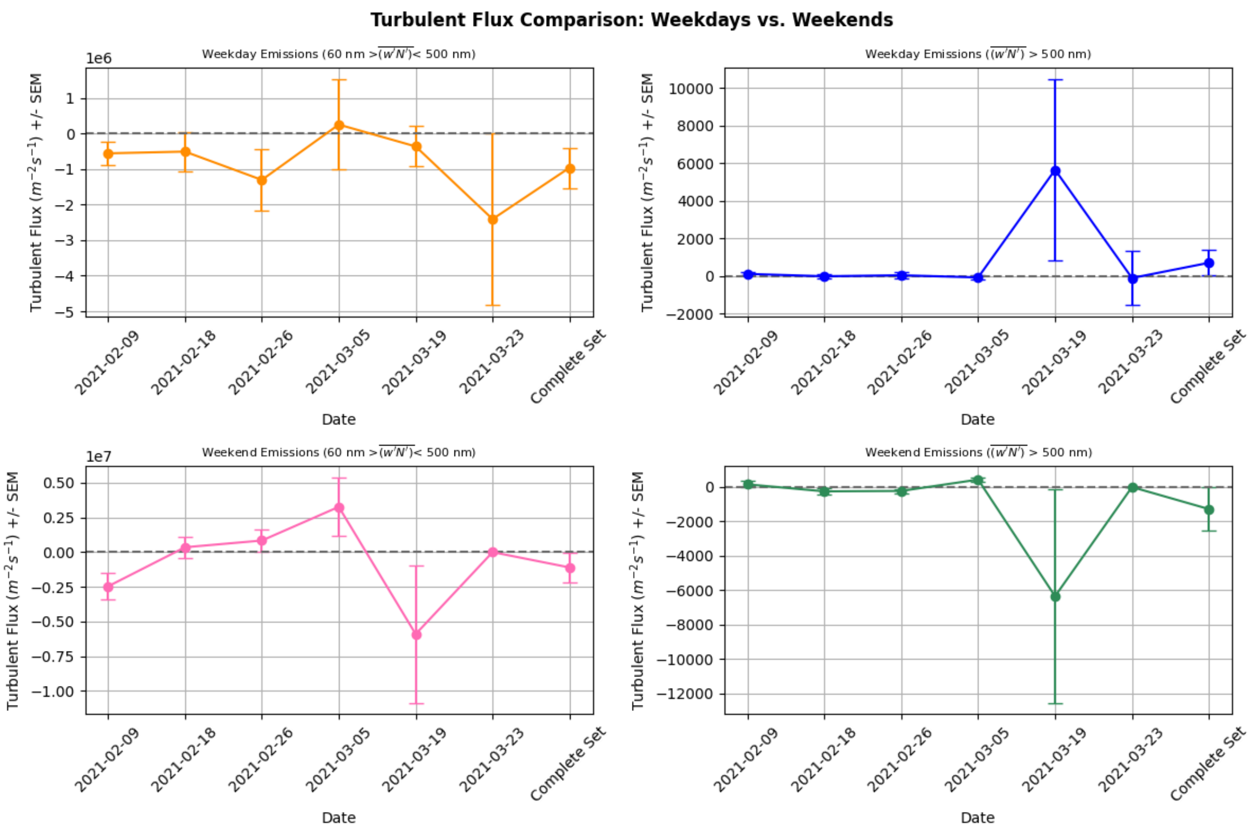

Figure 19: Comparative analysis of turbulent flux on weekdays and weekends. The four plots represent turbulent flux measurements for two different particle size ranges, greater than 500 nm (top row) and 60 nm to 500 nm (bottom row). The left column illustrates weekday emissions, and the right column represents weekend emissions. Error bars reflect the standard error of the mean (SE), providing an understanding of the variability and reliability of the data. The "Complete Set" on the x-axis represents the aggregate data across the sampled dates.

For the larger particles, once again, the 95% confidence interval spans both negative and positive values for the weekday and weekend, implying that the data are not indicating one consistent direction of flux. For the smaller particles the confidence interval spans -2.07×10^{6} to

1.52×10^5 for the weekday and -3.21×10^6 to 1.00×10^6 for the weekend. The average flux for the weekday for particles greater than 500 nm is -6.19×10^3 to 2.01×10^4 and -3.77×10^4 to 1.22×10^4 for the weekend. First analyzing the results from the weekend, even though the flux is negative indicating deposition, since the confidence interval is crosses zero, it indicates there is uncertainty suggesting that the data are not precise enough to confirm that there is definitive deposition. Furthermore, the span of the confidence interval suggests considerable variability in the measurement of turbulent flux. Similarly, the confidence interval for the weekday indicates a much larger range, indicating a very higher amount of uncertainty as to the turbulent flux.

The data presented for both particle sizes lacks the precision required to assess the effects of vehicle emissions on particle flux. The confidence intervals for the weekday and weekend measurement span both negative and positive values, failing to indicate a consistent direction of flux. The inconsistency indicates that the data are not robust enough to distinguish between deposition and emission or connect the values confidently to vehicular traffic. Due to the vast uncertainty in the measurements for analyzing according to weekday and weekend, it is difficult to draw a conclusion about the emission rates of vehicles. Another approach to further filter the data and analyze the particle flux during rush hour periods may lead to more definitive results. By reducing the temporal focus of the measurements to peak traffic periods there may be an enhancement in the precision and reliability of the data.

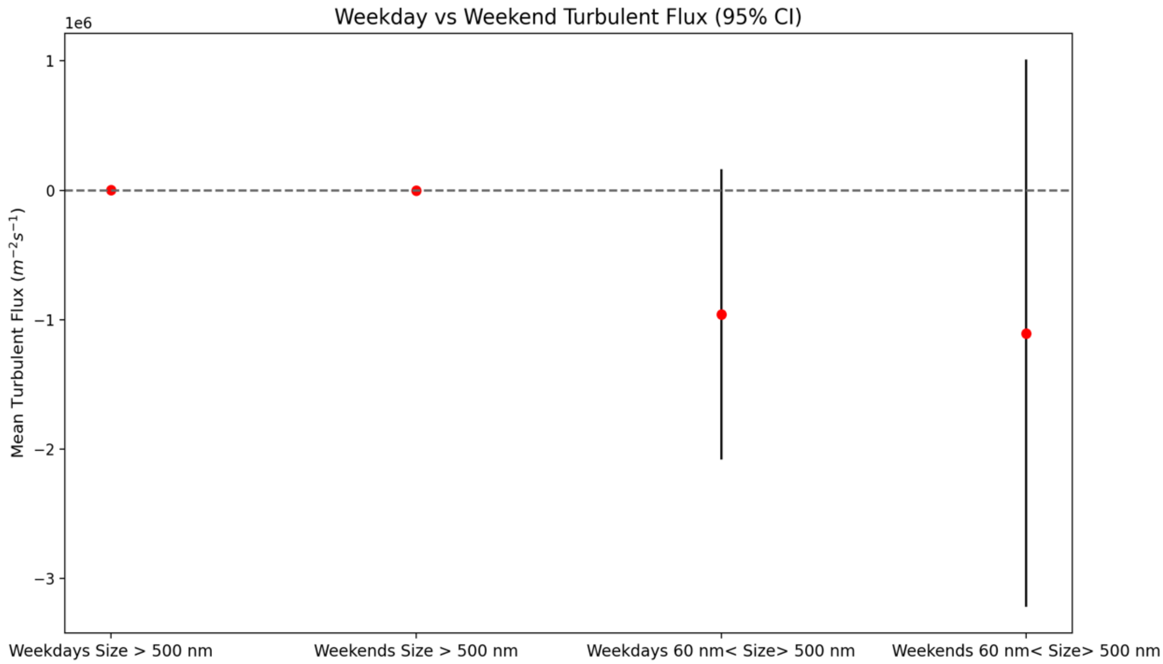

Figure 20: This graph shows the mean turbulent flux for particles larger than 500 nm, with error bars indicating the 95% confidence interval (CI) for each measurement. It contrasts the flux on weekdays with that on weekends, reflecting the variability in particle behavior between the two periods.

3.6: Comparative analysis of turbulent flux of rush hour

The composition of rush hour traffic, which includes the volume and assortment of vehicles, together with their velocity and acceleration, significantly influences roadway conditions [Batterman et al., 2015]. Variations in traffic flow over time serve as indicators of vehicular utilization, contribute to congestion, pose safety risks, and exert a considerable impact on the emissions and subsequent concentration of pollutants arising from traffic [Batterman et al., 2015]. In a 2019 study, Bateman identified the rush hour intervals in Toronto as being from 6 a.m. to 10 a.m. for the morning period and from 3:30 p.m. to 7 p.m. for the evening period. Comparative analysis with vehicle per hour data indicated a congruence with the periods mentioned, showing a synchronization of peak vehicle counts on Dufferin Street at 9 a.m. and 7 p.m. Table1 (section 3.1) outlines the average vehicle rates during weekday and weekend rush hours and during off-peaks

The weekday and weekend turbulent flux during rush hour can further isolate the effects of vehicular data in the sense that a higher flux compared with a higher vehicle count helps to associate the emission with vehicles. Table 6 highlights the average turbulent fluxes for the weekday vs. weekend and rush hour emission release for the study period.

Table 7: This table quantifies the turbulent flux for particle sizes at different morning and evening rush hour during weekdays and weekends. Values are given in particles/m²s with standard errors of the mean (SE) provided, offering a detailed view of the variability in particle flux related to daily and weekly traffic patterns.

Time of Day Flux SEM	60 nm < Particle Size < 500nm *Units: particles/m^2s*	Particle > 500 nm *Units: particles/m^2s*
Weekday Morning	9.06×10^5 SE: 1.75×10^6	5.59×10^2 SE: 701.97
Weekday Evening	-9.48×10^5 SE: 8.40×10^5	-4.40×10^2 SE: 1.14×10^3
Weekend Morning	-1.52×10^6 SE: 1.04×10^6	-1.40×10^3 SE: 1.48×10^4
Weekend Evening	-5.38×10^5 SE: 1.68×10^6	-8.30×10^2 SE: 1.38×10^3

During the weekday mornings the average emission for the research period remained positive indicating net emissions. Whereas the emissions in the evening had negative fluxes meaning deposition is dominant during the weekday evenings. The positive fluxes during the weekday mornings compared to the evening could be explained by the result of nocturnal accumulation of pollution. During the overnight period, the accumulation of pollution is common within the shallow boundary layer. However, as the sun rises and the boundary layer lifts and pollutants that were trapped are dispersed by the influx of fresh air from above, resulting in an increase in upward fluxes during the morning [Conte et al., 2017]. Considering that the weekend morning vehicle count is the lowest, yet the turbulent flux is greater than the evening, shows that there is a greater upwards flux during the morning period. The reduced vehicle activity during the weekend and the increase in deposition activity was also reported by Conte et al., 2017. In this study, both mornings and evenings are dominated by deposition. The increase in deposition can be due to the significantly lower number of vehicles on the road during the weekend allowing for more particles to settle which are from a source upwind. The study was conducted during the Covid-19 lockdown in Ontario. This is significant to the study because this changed the behaviour of vehicular traffic, causing a severe reduction in people's movement. Studies conducted Leece, Italy and Belin, Germany [Donateo et al., 2021; Straaten et al., 2022], analyzed the impacts of ultrafine particle concentrations and turbulent fluxes within urban areas during the Covid-19 lockdown. Both studies individually saw an increase in deposition with the sub-urban study areas acting as sinks which were previously sources. Donateo et al., 2021, reported that positive fluxes reduced by 61% and the Berlin study [Straaten et al., 2022] saw a reduction of 38%, which was indeed due to the significantly reduced number of vehicles on the road. These studies show how multiple urban areas have recorded deposition being more dominant due to lower levels of traffic.

Furthermore, the turbulent flux of smaller particles is significantly greater than that of larger particles, which can be due to more ultrafine particles from an external source on any given day but also possibly due to the setup of the roadway. With the traffic light being less than

100 m from the measurement locations, the frequent stop-and-go, acceleration, and congestion during rush hour, contributes to a higher value of ultrafine particles [Conte and Contini., 2019].

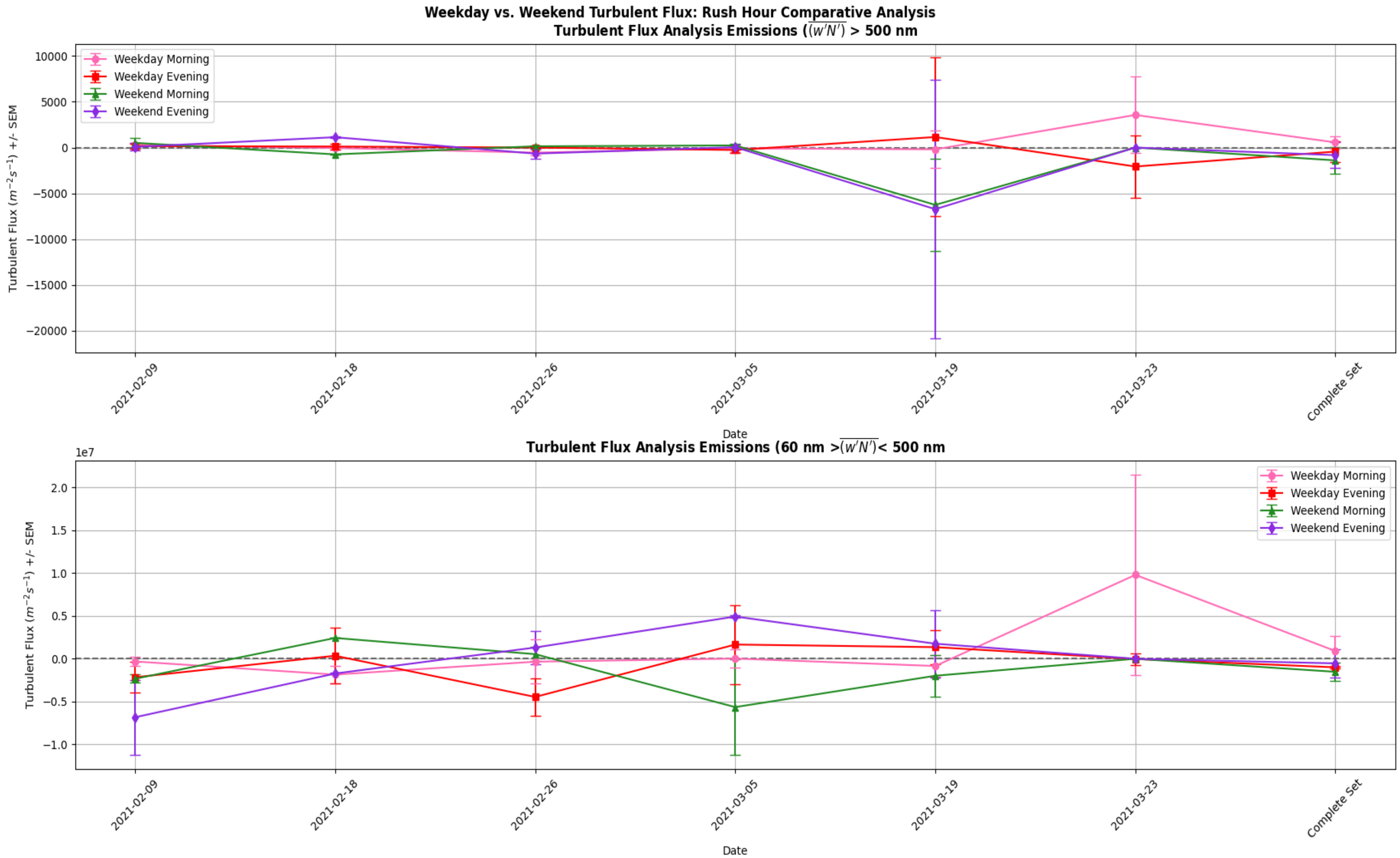

Figure 21: a) shows turbulent fluxes for particles larger than 500 nm, b) presents data for particles ranging from 60 nm to 500 nm. Turbulent flux for weekday mornings (red), weekday evenings (pink), weekend mornings (green), and weekend evenings (purple) are presented for both size ranges. Error bars indicate the standard error of the mean (SEM), providing a measure of data variability. The "Complete Set" data point represents an aggregate of all measurements, highlighting the overall trend and discrepancies in particle flux behavior during different periods of the week. Turbulent fluxes are for when the wind is from 180-270 degrees, showing crosswind of the road.

Figure 22 shows the confidence interval for the rush hour intervals. During the weekend, even though the flux is negative indicating deposition, since the confidence interval is crosses zero, it indicates there is uncertainty suggesting that the data is not precise enough to confirm that there is definitive deposition. Furthermore, the span of the confidence interval suggests considerable variability in the measurement of turbulent flux, especially for the weekend morning for particles > 500 nm and the weekend evening for smaller sized particles due to the greater uncertainty. With all the turbulent fluxes closer to the lower bound of the confidence interval it generally indicates deposition, but due to the significant uncertainty it cannot be concluded with certainty that it is deposition. Similarly, with smaller particles sizes, there is a variation between positive and negative fluxes but once again the confidence interval crossing zero, no concrete conclusion can be made.

This analysis highlights that on average during the weekday, the morning rush hour shows net emission while the evening rush hour period indicates net deposition. Similarly, the weekend rush hour period shows mainly characteristics of deposition. While morning rush hour on average shows a higher turbulent flux possibly due to the nocturnal accumulation of pollutants, which redistributes particles due to morning convective processes. The greater upward flux in the morning during the weekdays and weekends, with a reduced amount of vehicular movement compared to the other parts of the day suggests a complex interplay between meteorological parameters and local emission sources. With the increased variability within the data where for the weekend the measurements align with the lower bounds of the confidence interval suggesting potential deposition, the data does not allow for a conclusive result as to whether the source of the emission is from vehicular traffic. Instead, it is possible other external sources may be playing a greater role.

a)

b)

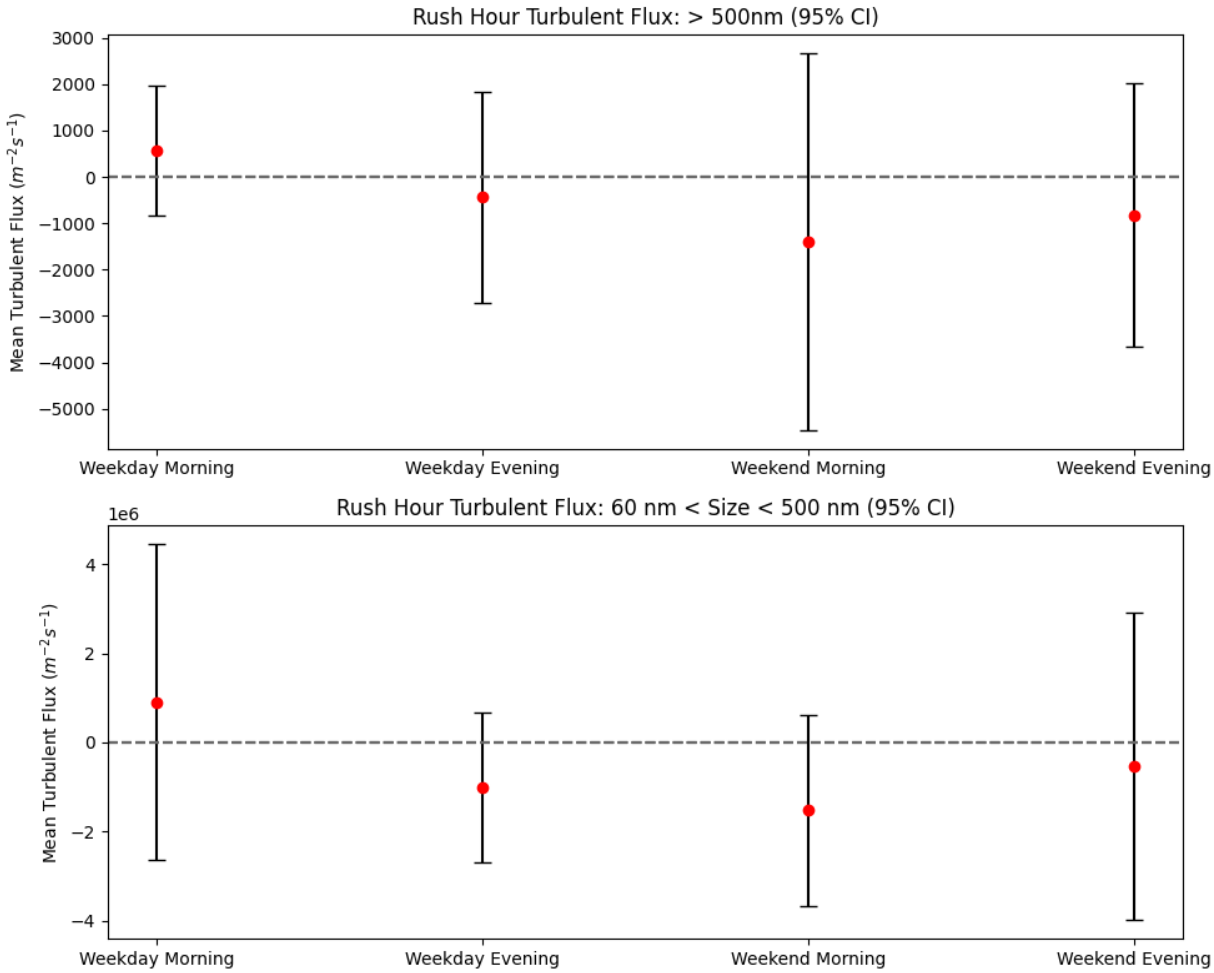

Figure 22: This graph shows the mean turbulent flux for particles larger than 500 nm, with error bars indicating the 95% confidence interval (CI) for each measurement. It presents the flux for the rush hour for weekday and weekend mornings and evenings, reflecting the variability in particle behavior between the two periods.

Traffic level vary on a daily basis, with some days involving work-related travel and other days not. Additionally, road closures and other traffic issues can change regularly, influencing vehicle emissions.

In this study, a diurnal cycle analysis was not conducted due to several factors. When analyzing turbulent fluxes by comparing weekdays versus weekends and rush hour periods, the confidence interval showed a large amount of uncertainty within the results, indicating no clear direction from the flux. The lack of distinct results from these analyses indicated that identifying the source of the flux was challenging, and a diurnal cycle analysis might not have provided additional clarity.

Furthermore, the rush hour periods during weekdays and weekends resemble a diurnal pattern to some extent. Although this study focused on an 8-hour section of the two rush hour periods rather than a full diurnal cycle, it still captured significant parts of the daily cycle. Straaten and Weber (2021) conducted a similar experiment, measuring turbulent flux using the eddy covariance method over a three-year period for particles ranging from 10 nm to 200 nm. Their study examined diurnal, seasonal, and annual patterns and found that the seasonal pattern was evident in the diurnal pattern for ultrafine particles. They also compared rush hour periods with weekday and weekend periods to analyze diurnal cycles, which was conducted within this study as well. Although this study did not include a comprehensive diurnal cycle analysis, the analysis of rush hour periods provided valuable insights into parts of the daily cycle. This approach allowed for a better understanding of vehicle emissions without the need for a full diurnal analysis.

Additionally, due to the lack of confidence in identifying the sources of the fluxes, a correlation between the turbulent flux and the vehicle could not be established. The flux varied greatly and attributing it to vehicles would have led to inaccurate results, as the flux could be influenced by other sources besides road vehicles.

Chapter 4: Conclusion and Future Work

Analyzing the variations in concentration, fluxes, and vehicle counts during weekdays, weekends, and rush hours can enhance the accuracy of the study and establish correlations among these variables.

When examining the relationship between vehicle rates, concentration, and turbulent fluxes, it was observed that despite higher vehicle rates during weekday evenings, there was no corresponding increase in concentration and turbulent flux for this period. In contrast, concentrations of both larger and smaller particles were higher during weekday mornings. This could be attributed to the nocturnal accumulation of pollutants, leading to increased upward flux as the boundary layer rises in the morning. However, for smaller particles, the confidence intervals were narrow and centered around zero, suggesting no significant net deposition or emission, and thus, no clear transport of these particles.

On the other hand, a distinct pattern was identified for smaller particles. The confidence interval for turbulent fluxes indicated more deposition than emission, contrasting with the background levels. Specifically, particles between 60 nm to 499 nm originated more from background sources than directly from the road, with the background characterized as wind coming from 90 to 170 degrees. This could be partly due to vehicular activity at a traffic light situated 100 m upwind, where stop-and-go conditions could lead to increased emissions of larger particles [Hagino et al., 2016].

Notably, during the week of March 19th to March 26th, the road contributed to a higher concentration of particles in both mornings and evenings, diverging from previous weeks where background sources were more prevalent. Although the confidence interval for rush hour turbulent flux is ambiguous, suggesting uncertainty in the flux direction, the average value is on the lower end and negative. This implies that on weekday evenings, the road likely functions as a deposition site.

Weekends also showed consistent deposition during morning and evening rush hours, potentially due to fewer vehicles compared to weekdays. Combined with contributions from the construction site, the road may serve as a sink rather than a source of particles. Such negative fluxes for large particles have been observed in other urban studies and could result from the dynamics of larger particles or traffic further from the measurement site [Conte and Contini, 2019]. Small particle negative fluxes have been recorded during studies in urban areas as well, such as during the Covid-19 lockdown in Italy. That study concluded that typical emission sources for ultrafine particles became sinks due to the drastic reduction in vehicles, allowing long-range transport to become the predominant source [Donateo et al., 2021].

While the exact vehicular patterns for this study are unknown, it's plausible that the road also acted as a sink during the study period, particularly if there were significant emissions upwind from the road. Consequently, it is apparent that deposition is more pronounced for particle sizes between 60 nm to 499 nm from the road, suggesting small particles settle on the road. However, due to significant uncertainty for weekday versus weekend and rush hour analyses, it is difficult to definitively link deposition and emission rates to traffic flow.

Future work following this study could focus on understanding the specific sources of particle emissions. Incorporating real-time traffic data, including vehicle types and speeds, would refine the understanding of how different vehicular behaviors contribute to particle fluxes. Long-term benefits of this research can include policymaking for urban planning and traffic management, aiming to reduce vehicular emissions and improve air quality. Additionally, considering how difficult it is to understand dispersion within an urban area, measuring turbulent flux and emissions from three different heights within an urban canopy can help to better understand the vertical distribution and dispersion patterns of vehicular traffic emissions. This will also help to assess which particle sizes are present higher in the atmosphere, identifying what is coming from the road under analysis and what is coming from upwind. This approach will enhance the accuracy of air quality models and provide insights into the impact of urban structures on pollutant dispersion. Such studies can also guide the design of green infrastructure that mitigates pollution in high-traffic areas, contributing to healthier urban environments

Appendix A: Deriving Boundary Layer Height.

There is no one direct approach that can be proposed to determine boundary layer heights, h. There are many comprehensive approaches proposed, but a "non-exhaustive" approach was provided by Klijun et al for the different conditions.

For stable and neutral conditions, Nieuwstadt (1981) proposed an interpolation formula as follows:

$$h = \frac{L}{3.8}[-1 + (1 + 2.28\frac{u_*}{fL})^{1/2} \quad (A1)$$

Where L is the Obukhov length, u_* is the friction velocity, and $f = 2\Omega sin\phi$ is the Coriolis parameter (with ϕ is the latitude and Ω is the angular velocity).

For near neutral conditions, for large L, equation B1 becomes:

$$h_n = c_n \frac{u_*}{|f|} \quad (A2)$$

Hanna and Chang (1993) recommend c_n=0.3. A2 is only valid for the stability of the free atmosphere between 10 <$N|f|^{-1}$< 70, where N is the Brunt-Viäisälä frequency which is defined as $N = (\frac{g}{T}\frac{dT}{dz})^{1/2}$. If L is still very large A2 becomes:

$$h_{nn} = (c_{nn}\frac{u_*}{|fN|^{1/2}}) \quad (A3)$$

Where c_{nn}= 1.36.

For strongly stable conditions Zilitinkevich(1972) proposed,

$$h_s = c_s(\frac{u_* L}{|f|})^{1/2} \quad (A4)$$

For which the applicability range is between 3<< $\frac{u_* L}{|f|}$<<100. The parameter of $c_s \approx 0.4$ was suggested by the numerical parameters in A1 for the limit of very strong stability. However, Zilitinkevich et al. (2007) proposed $c_s \approx 0.3$ based on LES results.

In convective conditions, the boundary layer height cannot be determined solely based on the diurnal cycle of the surface heat flux and thus must be integrated using a prognostic expression. The integration starts at sunrise when the initial height is diagnosed using expressions A1 through A4 before the surface heat flux becomes positive. The slab model of Batchvarova and Gryning(1991) provides the following equation for the rate of change for the boundary layer height, which is implicit in h and may be solved iteratively or using h(t_i) to determine the rate of change to yield h(t_{i+1}):

$$\frac{dh}{dt} = \frac{\overline{(w'T')}_0}{\gamma}\left[\left(\frac{h^2}{(1+2A)h-2BkL}\right) + \frac{Cu^2{}_*T}{\gamma g(1+A)h-BkL}\right]^{-1} \quad \text{(A5)}$$

γ is the gradient potential temperature above the convective boundary layer. γ is often not available for typical application and can be approximated by a constant parameter. A, B, C are derived from similar relations in the convective boundary layer that have been implemented to find the growth rate of its heights with A=0.2, B=2.5, and C=8.

References

Alshetty, Dheeraj, and S.M. Shiva Nagendra. "Impact of Vehicular Movement on Road Dust Resuspension and Spatiotemporal Distribution of Particulate Matter during Construction Activities." *Atmospheric Pollution Research*, vol. 13, no. 1, 2 Nov. 2021, p. 101256., https://doi.org/10.1016/j.apr.2021.101256.

Ao, X., Grimmond, C., Chang, Y., Liu, D., Tang, Y., Hu, P., Wang, Y., Zou, J., and Tan, J.: Heat, water and carbon exchanges in the tall megacity of Shanghai: challenges and results, Int. J. Climatol., 36, 4608–4624, https://doi.org/10.1002/joc.4657, 2016.

Baensch-Baltruschat, B.; Kocher, B.; Stock, F.; Reifferscheid, G. Tyre and road wear particles (TRWP)—A review of generation, properties, emissions, human health risk, ecotoxicity, and fate in the environment. Sci. Total Environ. 2020, 733, 137823.

Barlow, Janet F., et al. "A wind-tunnel study of flow distortion at a meteorological sensor on top of the BT tower, London, UK." *Journal of Wind Engineering and Industrial Aerodynamics*, vol. 99, no. 9, Sept. 2011, pp. 899–907, https://doi.org/10.1016/j.jweia.2011.05.001.

Bateman, Chris. "When Exactly Is Rush Hour in Toronto?" *blogTO*, blogTO, 24 Mar. 2019, www.blogto.com/city/2014/04/when_exactly_is_rush_hour_in_toronto/#:~:text=The%20first%2C%20between%208%20a.m.,the%20TTC%20is%20most%20claustrophobic.

Batterman, Stuart, et al. "Temporal variation of traffic on highways and the development of accurate temporal allocation factors for air pollution analyses." *Atmospheric Environment*, vol. 107, Apr. 2015, pp. 351–363, https://doi.org/10.1016/j.atmosenv.2015.02.047.

Brugge, Doug, et al. "Highway proximity associations with blood markers of inflammation: Evidence for a role for il-1β." *Journal of Toxicology and Environmental Health, Part A*, vol. 76, no. 3, Feb. 2013, pp. 201–205, https://doi.org/10.1080/15287394.2013.752325.

Brümmer, Burghard, et al. "Atmospheric boundary layer measurements at the 280 m high Hamburg weather mast 1995-2011: Mean annual and diurnal cycles." *Meteorologische Zeitschrift*, vol. 21, no. 4, 1 Aug. 2012, pp. 319–335, https://doi.org/10.1127/0941-2948/2012/0338.

"California Air Resources Board." *Inhalable Particulate Matter and Health (PM2.5 and PM10) | California Air Resources Board*, ww2.arb.ca.gov/resources/inhalable-particulate-matter-and-health#:~:text=Long%2Dterm%20(months%20to%20years,lung%20function%20growth%20in%20children. Accessed 4 July 2024.

Camatini, M.; Crosta, G.F.; Dolukhanyan, T.; Sung, C.; Giuliani, G.; Corbetta, G.M.; Cencetti, S.; Regazzoni, C. Microcharacterization and identification of tire debris in heterogeneous laboratory and environmental specimens. Mater. Charact. 2001, 46, 271–283.

Carlier, Mathilde. “Canadian Electric Vehicle Sales 2021.” *Statista*, 29 Sept. 2023, www.statista.com/statistics/665870/sales-of-plug-in-light-vehicles-in-canada/#:~:text=In%202021%2C%20Canada’s%20auto%20dealers,units%20between%202010%20and%202021.

Carlier, Mathilde. “Italy: Market Share of Battery Electric Cars 2021.” *Statista*, 19 Dec. 2023, www.statista.com/statistics/736887/market-share-of-electric-cars-registered-in-italy/.

“City of Toronto Traffic Data Shows More People Staying Home to Fight Covid-19.” *City of Toronto*, 22 Jan. 2021, www.toronto.ca/news/city-of-toronto-traffic-data-shows-more-people-staying-home-to-fight-covid-19/#:~:text=This%20data%20shows%20that%20daily,the%20latest%20measures%20were%20introduced.

Conte, M., and Contini, D.. “Size-Resolved Particle Emission Factors of Vehicular Traffic Derived from Urban Eddy Covariance Measurements.” *Environmental Pollution*, Elsevier, 11 May 2019, www.sciencedirect.com/science/article/abs/pii/S0269749118357543.

Dahl, A.; Gharibi, A.; Swietlicki, E.; Gudmundsson, A.; Bohgard, M.; Ljungman, A.; Blomqvist, G.; Gustafsson, M. Trafficgenerated emissions of ultrafine particles from pavement-tire interface. Atmos. Environ. 2006, 40, 1314–1323.

Deventer, Malte Julian, et al. “Size-resolved flux measurement of sub-micrometer particles over an urban area.” *Meteorologische Zeitschrift*, vol. 22, no. 6, 1 Dec. 2013, pp. 729–737, https://doi.org/10.1127/0941-2948/2013/0441.

Deshmukh P, Isakov V, Venkatram A, Yang B, Zhang KM, Logan R, Baldauf R. The effects of roadside vegetation characteristics on local, near-road air quality. Air Qual Atmos Health. 2019 Mar 11;12:259-270. PMID: 32636958; PMCID: PMC7339705.

Donateo, Antonio, et al. “Impact on ultrafine particles concentration and turbulent fluxes of SARS-COV-2 lockdown in a suburban area in Italy.” *Atmosphere*, vol. 12, no. 3, 21 Mar. 2021, p. 407, https://doi.org/10.3390/atmos12030407.

Fauser, P.; Tjell, J.C.; Mosbaek, H.; Pilegaard, K. Tire-tread and bitumen particle concentrations in aerosol and soil samples. Pet. Sci. Technol. 2002, 20, 127–141.

Foitzik, M.-J.; Unrau, H.-J.; Gauterin, F.; Dörnhöfer, J.; Koch, T. Investigation of ultra fine particulate matter emission of rubber tires. Wear 2018, 394–395, 87–95.

Foken, Thomas. *Micro-Meteorology* . Springer-Verlag, 2008.

Fussell, Julia C., et al. “A review of road traffic-derived Non-Exhaust particles: Emissions, physicochemical characteristics, health risks, and mitigation measures.” *Environmental Science & Technology*, vol. 56, no. 11, 25 May 2022, pp. 6813–6835, https://doi.org/10.1021/acs.est.2c01072.

Gordon, Mark, et al. “Measured and modeled variation in pollutant concentration near roadways.” *Atmospheric Environment*, vol. 57, 2012, pp. 138–145, https://doi.org/10.1016/j.atmosenv.2012.04.022.

Hagen, F. H. F. zum, et al. "Study of Brake Wear Particle Emissions: Impact of Braking and Cruising Conditions." *Environmental Science & Technology*, vol. 53, no. 9, 2019, pp. 5143-5150.

Hagino, Hiroyuki, et al. “Laboratory Testing of Airborne Brake Wear Particle Emissions Using a Dynamometer System under Urban City Driving Cycles.” *Atmospheric Environment*, vol. 131, 12 Feb. 2016, pp. 269–278, https://doi.org/10.1016/j.atmosenv.2016.02.014.

Held, Klemm, 2006. Direct measurement of turbulent particle exchange with a twin CPC eddy covariance system. Atmos. Environ. 40 (Suppl. 1), S92eS102.

Hildemann LM, Markowski GR, Cass GR. Chemical-composition of emissions from urban sources of fine organic aerosol. Environ Sci Technol 1991;25:744–59.

Hinds, W. C. (1999). Aerosol Technology. J. Wiley

Hsieh, Cheng-I, et al. “An approximate analytical model for footprint estimation of scalar fluxes in thermally stratified atmospheric flows.” *Advances in Water Resources*, vol. 23, no. 7, June 2000, pp. 765–772, https://doi.org/10.1016/s0309-1708(99)00042-1.

Iijima, A., et al. "Particle Size and Composition Distribution Analysis of Automotive Brake Abrasion Dusts for the Evaluation of Antimony Sources of Airborne Particulate Matter." *Atmospheric Environment*, vol. 41, no. 21, 2007, pp. 4908-4919.

Järvi, Leena, et al. “Uncertainty of eddy covariance flux measurements over an urban area based on Two Towers.” *Atmospheric Measurement Techniques*, vol. 11, no. 10, 2 Oct. 2018, pp. 5421–5438, https://doi.org/10.5194/amt-11-5421-2018.

Keogh, Stephanie, et al. “The energy budget of the urban surface: Two locations in Dublin.” *Irish Geography*, vol. 45, no. 1, Mar. 2012, pp. 1–23, https://doi.org/10.1080/00750778.2012.689182.

Klippenstein, Matthew (February 2016). *"Canadian Plug-in Electric Vehicle Sales"*. Green Car Reports. *Retrieved 2016-02-07.Tesla Model S sales figures from IHS data.*

Kljun, N., et al. “A Simple Two-Dimensional Parameterisation for Flux Footprint Prediction (FFP).” *Geoscientific Model Development*, vol. 8, no. 11, 2015, pp. 3695– 3713., https://doi.org/10.5194/gmd-8-3695-2015.

Kreider, M.L.; Panko, J.M.; McAtee, B.L.; Sweet, L.I.; Finley, B.L. Physical and chemical characterization of tire-related particles: Comparison of particles generated using different methodologies. Sci. Total Environ. 2010, 408, 652–659.

Kumar, Prashant, et al. “Dynamics and dispersion modelling of nanoparticles from road traffic in the urban atmospheric environment—a review.” *Journal of Aerosol Science*, vol. 42, no. 9, 16 June 2011, pp. 580–603, https://doi.org/10.1016/j.jaerosci.2011.06.001.

Kwak, J.; Lee, S.; Lee, S. On-road and laboratory investigations on non-exhaust ultrafine particles from the interaction between the tire and road pavement under braking conditions. Atmos. Environ. 2014, 97, 195–205.

Kwon, HS., Ryu, M.H. & Carlsten, C. Ultrafine particles: unique physicochemical properties relevant to health and disease. *Exp Mol Med* **52**, 318–328 (2020). https://doi.org/10.1038/s12276-020-0405-1

Lamaud, E., Chapuis, A., Fontan, J., Serie, E., 1994. Measurements and parameteri- zation of aerosol dry deposition in a semi-arid area. Atmos. Environ. 28, 2461e2471.

León-Mejía, G., Silva, L.F., Civeira, M.S., Oliveira, M.L.S., Machado, M., Villela, I.V., Hartmann, A., Premoli, S., Corrêa, D.S., Silva, L., Henriques, J.A.P., 2016. Cytotoxicity and genotoxicity induced by coal and coal fly ash particles samples in V79 cells. Environ. Sci. Pollut. Res. 23, 24019–24031. https://ezproxy.cuc.edu.co:2067/10.1007/ s11356-016-7623-z.

León-Mejía, G., Machado, M.N., Okuro, R.T., Silva, L.F., Telles, C., Dias, J., Niekraszewicz, L., Da Silva, J., Henriques, J.A.P., Zin, W.A., 2018. Intratracheal instillation of coal and coal fly ash particles in mice induces DNA damage and translocation of metals to extrapulmonary tissues. Sci. Total Environ. 625, 589–599. https://doi.org/10.1016/j. scitotenv.2017.12.283.

Liu, H. Z., et al. “Four-year (2006–2009) eddy covariance measurements of co₂ Flux over an urban area in Beijing.” *Atmospheric Chemistry and Physics*, vol. 12, no. 17, 3 Sept. 2012, pp. 7881–7892, https://doi.org/10.5194/acp-12-7881-2012.

Mathissen, M.; Scheer, V.; Vogt, R.; Benter, T. Investigation on the potential generation of ultrafine particles from the tire–road interface. Atmos. Environ. 2011, 45, 6172–6179.

Matthaios, Vasileios N., et al. “Quantifying factors affecting contributions of roadway exhaust and non-exhaust emissions to ambient PM10–2.5 and PM2.5–0.2 particles.” *Science of The Total Environment*, vol. 835, 2022, p. 155368, https://doi.org/10.1016/j.scitotenv.2022.155368.

Miller, Stefan. *An Investigation of Turbulence and Diffusion within Vehicles Wakes on Road Measurement Using an Instrument Mobile Car and a Stationary Roadside Monitoring System*. 2022. York University, Doctoral Dissertation.

Miller, Stefan J., et al. “A study of the spatial variation of vehicle-induced turbulence on highways using measurements from a mobile platform.” *Boundary-Layer Meteorology*, vol. 171, no. 1, 3 Jan. 2019, pp. 1–29, https://doi.org/10.1007/s10546-018-0416-9.

McMurry, P. H., Shepherd, M. F. & Vickery, J. S. *Particulate Matter Science for Policy Makers: a NARSTO Assessment* (Cambridge University Press, 2004).

Moore, R. H., Wiggins, E. B., Ahern, A. T., Zimmerman, S., Montgomery, L., Campuzano Jost, P., Robinson, C. E., Ziemba, L. D., Winstead, E. L., Anderson, B. E., Brock, C. A., Brown, M. D., Chen, G., Crosbie, E. C., Guo, H., Jimenez, J. L., Jordan, C. E., Lyu, M., Nault, B. A., … Wang, J. (2021). Sizing response of the ultra–high sensitivity aerosol spectrometer (UHSAS) and Laser Aerosol Spectrometer (LAS) to changes in submicron aerosol composition and refractive index. Atmospheric Measurement Techniques, 14(6), 4517–4542. https://doi.org/10.5194/amt–14–4517–2021

Nemitz, E., Gallagher, M.W., Duyzer, J.H., Fowler, D., 2002. Micrometeorological measurements of particle deposition velocities to moorland vegetation. Q. J. Roy. Meteorol. Soc. 128, 2281e2300.

Nordbo, Annika, et al. “Intra-city variation in urban morphology and turbulence structure in Helsinki, Finland.” *Boundary-Layer Meteorology*, vol. 146, no. 3, 11 Oct. 2012, pp. 469–496, https://doi.org/10.1007/s10546-012-9773-y.

Oke, T. R., et al. *Urban Climates*. Cambridge University Press, 2017.

“OpenCV Tutorial: Opencv Using Python - Javatpoint.” *Www.javatpoint.com*, https://www.javatpoint.com/opencv.

Pant, Pallavi, and Harrison, R. “Estimation of the Contribution of Road Traffic Emissions to Particulate Matter Concentrations from Field Measurements: A Review.” *Atmospheric Environment*, vol. 77, 11 Mar. 2013, pp. 78–97., https://doi.org/10.1016/j.atmosenv.2013.04.028.

Park, J., et al. "Analysis of Wear Induced Particle Emissions from Brake Pads during the Worldwide Harmonized Light Vehicles Test Procedure (WLTP)." *Wear*, vol. 466-467, 2021, p. 203539.

Pellerin, G., Maro, D., Damay, P., Gehin, E., Connan, O., Laguionie, P., Hebert, D., Solier, L., Boulaud, D., Lamaud, E., Charrier, X., 2017. Aerosol particle dry deposition velocity above natural surfaces: quantification according to the particle’s diameter. J. Aerosol Sci. 114, 107e117.

Pérez, N., Pey, J., Cusack, M., Reche, C., Querol, X., Alastuey, A., Viana, M., 2010. Variability of particle number, black carbon, and PM10, PM2.5, and PM1 levels and speciation: in- fluence of road traffic emissions on urban air quality. Aerosol Sci. Technol. 44, 487–499.

Ramírez, O., Da Boit, K., Blanco, E., Silva, L.F.O., 2020. Hazardous thoracic and ultrafine particles from road dust in a Caribbean industrial city. Urban Clim. 33, 100655. https:// doi.org/10.1016/j.uclim.2020.100655.

Rogge WF, Hildemann LM, Mazurek MA, Cass GR. Sources of fine organic aerosol. 3. Road dust, tire debris, and organometallic brake lining dust: roads as sources and sinks. Environ Sci Technol 1993;27:1892.

Roser, Max. "Data Review: How Many People Die from Air Pollution?" *Our World in Data*, 25 Nov. 2021, https://ourworldindata.org/data-review-air-pollution-deaths.

Roth, M. "Review of atmospheric turbulence over cities." *Quarterly Journal of the Royal Meteorological Society*, vol. 126, no. 564, Apr. 2000, pp. 941–990, https://doi.org/10.1002/qj.49712656409.

Seinfeld, J.H. "Tropospheric chemistry and composition | aerosols/particles." *Encyclopedia of Atmospheric Sciences*, 2015, pp. 182–187, https://doi.org/10.1016/b978-0-12-382225-3.00438-2.

Sherman, D.J., et al. "14.17 Electronic Measurement Techniques for Field Experiments in Process Geomorphology." *Treatise on Geomorphology*, Academic Press, 5 Mar. 2013, https://www.sciencedirect.com/science/article/pii/B9780123747396004012

"Sonic Tilt Corrections." *Sonic Tilt Corrections | Earth Observing Laboratory*, NSF, https://www.eol.ucar.edu/content/sonic-tilt-corrections.

Spurny, K. R. On the physics, chemistry and toxicology of ultrafine anthropogenic, atmospheric aerosols (UAAA): new advances. *Toxicol. Lett.* **96–97**, 253–261 (1998).

Straaten, Agnes, et al. "Significant reduction of ultrafine particle emission fluxes to the urban atmosphere during the COVID-19 lockdown." *Science of The Total Environment*, vol. 838, Sept. 2022, p. 156516, https://doi.org/10.1016/j.scitotenv.2022.156516.

Straaten, Agnes, and Stephan Weber. "Measurement report: Three years of size-resolved eddy-covariance particle number flux measurements in an urban environment." *Atmospheric Chemistry and Physics*, vol. 21, no. 24, 23 Dec. 2021, pp. 18707–18726, https://doi.org/10.5194/acp-21-18707-2021.

Thomas, Adam E., et al. "Automotive braking is a source of highly charged aerosol particles." *Proceedings of the National Academy of Sciences*, vol. 121, no. 13, 11 Mar. 2024, https://doi.org/10.1073/pnas.2313897121.

Thorpe, Alistair J., et al. "Estimation of particle resuspension source strength on a major London Road." *Atmospheric Environment*, vol. 41, no. 37, 2007, pp. 8007–8020, https://doi.org/10.1016/j.atmosenv.2007.07.006.

Thorpe, Alistair, and Roy M. Harrison. "Sources and Properties of Non-Exhaust Particulate Matter from Road Traffic: A Review." *Science of The Total Environment*, vol. 400, no. 1–3, 16 July 2008, pp. 270–282, https://doi.org/10.1016/j.scitotenv.2008.06.007.

"Trends in Fuel Type of New Cars between 2015 and 2016, by Country." *European Automobile Manufacturers Association*, 26 Aug. 2021, www.acea.auto/figure/trends-in-fuel-type-of-new-cars-between-2015-and-2016-by-country/.

Ultra-High Sensitivity Aerosol Spectrometer (UHSAS) DOC-0210 Rec E-4, Droplet Measurement Technologies, Longmont, CO, USA, 2017, pp.8-12. Accessed: MAR 2023 [online]. Available: https://dropletmeasure.wpenginepowered.com/wp-content/uploads/2020/02/DOC-0210-Rev-E-4-UHSAS-Manual.pdf

"Ultrasonic Anemometer Probe Styles." *Applied Technologies, Inc.*,https://www.apptech.com/probe-styles/.

Vesh, Hayley. "Report: The Most Popular Fuel Types among Used Vehicles in Canada." *LowestRates*, 28 Oct. 2021, www.lowestrates.ca/blog/reports/most-popular-fuel-type-used-vehicles-canada.

Wilczak, James M., Oncley, Steven P., and Stage, Steven A., National Oceanic and Atmospheric Administration, Environmental Research Laboratories, Environmental Technology Laboratory, Boulder, CO 80303, U.S.A.; National Center for Atmospheric Research, Boulder, CO 80303, U.S.A.; Innovative Emergency Management, Baton Rouge, LA 70809, U.S.A.

Willis, Megan D., et al. "Aircraft-based measurements of High Arctic springtime aerosol show evidence for vertically varying sources, transport and composition." *Atmospheric Chemistry and Physics*, vol. 19, no. 1, 3 Jan. 2019, pp. 57–76, https://doi.org/10.5194/acp-19-57-2019.

Wood, C. R., et al. "Turbulent flow at 190 m height above London during 2006–2008: A climatology and the applicability of similarity theory." *Boundary-Layer Meteorology*, vol. 137, no. 1, 20 June 2010, pp. 77–96, https://doi.org/10.1007/s10546-010-9516-x.

Yan, H.; Zhang, L.; Liu, L.; Wen, S. Investigation of the external conditions and material compositions affecting the formation mechanism and size distribution of tire wear particles. Atmos. Environ. 2021, 244, 118018.

Zhang, K., Batterman, S., 2013. Air pollution and health risks due to vehicle traffic. Sci. Total Environ. 450–451, 307–316.

Zhang, K. Max, and Anthony S. Wexler. "Evolution of particle number distribution near roadways—part I: Analysis of Aerosol Dynamics and its implications for engine emission measurement." *Atmospheric Environment*, vol. 38, no. 38, Dec. 2004, pp. 6643–6653, https://doi.org/10.1016/j.atmosenv.2004.06.043.

Zhong, C.; Sun, J.; Zhang, J.; Liu, Z.; Fang, T.; Liang, X.; Yin, J.; Peng, J.; Wu, L.; Zhang, Q.; et al. Characteristics of Vehicle Tire and Road Wear Particles' Size Distribution and Influencing Factors Examined via Laboratory Test. Atmosphere 2024, 15, 423. https://doi.org/10.3390/atmos15040423